ULTRA-DENSE MOTION CAPTURE ALGORITHM FOR BREAST BIOMECHANICAL MODELLING IN DESIGN OF SPORTS BRAS

QILONG LIU

MPhil

The Hong Kong Polytechnic University

2024

The Hong Kong Polytechnic University
School of Fashion and Textiles

Ultra-dense Motion Capture Algorithm for Breast Biomechanical Modelling in Design of Sports Bras

Qilong Liu

A thesis submitted in partial fulfillment
of the requirements for the degree
of Master of Philosophy

August 2023

Certificate of originality

I hereby declare that this thesis is my own work and that, to the best of my knowledge and belief, it reproduces no material previously published or written, nor material that has been accepted for the award of any other degree or diploma, except where due acknowledgement has been made in the text.

	(Signed)
Qi-long Liu	(Name of student)

Abstract

This thesis presents a comprehensive approach to facilitate breast biomechanics research and ergonomic sports bra design. The study involves three main components: dynamic 4D scanning of the female subject during running, dense tracking of breast deformation, and finite element modeling with material properties fine-tuning using 4D scanning data. The innovative use of 4D scanning technology captures whole-surface information of the human body during dynamic activities, providing high-temporal and spatial resolutions mesh data for analysis. Based on the anthropometric landmarks labelled from the 4D scanning sequence, the overall trajectories and the accumulated regional displacement of the breast soft tissues, as well as the distribution of deformation intensity can be precisely analyzed. Results indicated that the accumulated trajectory lengths of different landmarks range from 50 cm to 80 cm. Of which, the vertical and lateral swinging are the primary movement trends of the breasts during running. The large trajectory differences (48.6%) amongst the landmarks also confirm the highly nonlinear deformation patterns of the breasts during dynamic motion.

A robust dense tracking method, the Ultra-dense Motion Capture (UdMC) algorithm, is proposed to capture the dense whole-surface deformation profile of the breasts, advancing the traditional motion capture technology from the sparse landmark level to the dense surface level. Comprehensive evaluation shown that our approach significantly outperforms previous works in accuracy, consistency, and efficiency. With reference to the complete 120 fps dataset, the average errors are found as 0.43cm for the control-landmarks and 0.78cm for the non-control (arbitrary) points. As compared to the traditional approach, the calculation speed of the proposed UdMC algorithm is 40-200 times faster.

Lastly, a subject-specific finite element (FE) model is constructed and fine-tuned with the dense deformation profile captured by UdMC, making it capable to align with the realistic breast behavior more reliably. To facilitate efficient determination of the subject-specific Mooney-Rivlin material parameters, the principle parameters inflation scheme was proposed

to transform the optimization problem from the 5 dimensional space search to the 2 dimensional space search. This FE breasts model has successfully simulated and predicted the characteristics and response of the breasts when wearing different sports bra with varying design factors, which has significant application value in breasts soft tissue biomechanics research as well as validating and optimizing sports bras prototype designs.

Publications arising from the thesis

Liu, Q. L., Yick, K. L., Chan, K. C., Wong, S. T., & Ng, S. P. (2022). Sports bra pressure: Effect on core body temperature and comfort sensation. *13th International Conference on applied Human Factors and Ergonomics, AHFE 2022. New York, USA, 24-28 July 2022.* https://doi.org/10.54941/ahfe1001991

Liu, Q. L., Yick, K. L., Sun, Y., & Yip, J. (2023). Ultra-dense motion capture: An exploratory full-automatic approach for dense tracking of breast motion in 4d. *PLoS One. Under Review.*

Acknowledgements

First and foremost, I would like to express my deepest gratitude to my chief supervisor, Prof. Kit-lun Yick. Her unwavering support throughout the journey of pursuing a Master of Philosophy degree has been invaluable. Despite the inevitable hindrances and setbacks that came along the way, her faith in me and my project never wavered.

I am immensely grateful to both my co-supervisors, Prof. Joanne Yip, and Dr. Yue Sun. Dr. Yue Sun's previous work has laid down a solid foundation for mine; the Finite Element (FE) part of this thesis extends her Ph.D research. Her guidance on FE modelling was instrumental in shaping this work. Regular discussion sessions with Prof. Joanne Yip were not only helpful but also inspiring due to the valuable feedback she provided.

My heartfelt thanks go out to post-doc Dr. Qiu-qiong Shi and senior PhD student Li-ying Zhang as well. As a newcomer in academia, their advice and guidance were indispensable in helping me understand what it means to design, prepare, carry out a research project as well as report it through formally and clearly written manuscripts.

This work would not have been possible without financial support from various sources: The Hong Kong Polytechnic University Research Studentship; Innovation and Technology Fund (Project: ITS/043/20); Research Grant Council (Project: 15606922); Laboratory for Artificial Intelligence in Design (Project: RP1-2).

Before I conclude, it is essential to express my deepest gratitude towards my parents. Their unwavering love and support have been the cornerstone of my journey. While they may not have directly guided me in this research, their constant encouragement has always propelled me forward

during challenging times. They've made countless sacrifices over the years to ensure that I had every opportunity for success. Even though we were physically separated by miles, their words of motivation and reassurance were always with me.

Last but certainly not least, I want to thank Shu-ying - my rock during these challenging times. Though it may be a little bit odd to hear words like "passing through darkness and lights" from the mouth of a 20+ years old lad, I must say I wouldn't know where I would be without her by my side crossing all those days of bottlenecks, stress, and uncertainties - both in research and in life. All those camera calls during the periods of the Covid-19 epidemic are so vivid in my memory - though we were thousands of miles away and there were traveling restrictions between us, I could feel our hearts beat together.

Table of Contents

List of Figures

List of Tables

Chapter 1

Introduction

1.1 Background

Today, athleisure and activewear have become important segments in the global apparel industry due to the ever-increasing health and fitness concerns. Since the structure of the breasts provides little anatomic support, when there is breast motion (caused by torso movement), the skin stretches and the breasts show viscous damping and hyper-elastic behaviors, which may lead to negative effects (McGhee & Steele, 2010). To protect the structure of the breasts and reduce the risk of breast sagging, the sports bras are designed for the female customers and it can also increase confidence and improve performances (Page & Steele, 1999; Starr et al., 2005; White et al., 2009). However, the forces transferred from the torso during locomotion are highly complex. Moreover, considering the unique rheological and biomechanical behaviors of the breast tissues of each female user, it's very challenging to effectively control the breast motion (Gefen & Dilmoney, 2007; Haake & Scurr, 2010, 2011) without applying excessive pressure onto the breasts. To date, the breast displacement, elevation, acceleration, and bra-breast contact pressure caused by physical activity still cannot be effectively controlled, which leads to risk factors of breast discomfort, pain, and sagging.

Breasts consist of skin, fat, and glandular tissues, with a structure that has a complex tree-like architecture with both elastic and viscous components that contribute to the complex deformation pattens of the breasts. To

develop more ergonomically desired sports bra, it's vital to understand the dynamic breast deformation patterns during active activities. Though has gathered lots of information on the breasts dynamic deformation patterns, previous studies are typically based on the MoCap systems (Zhang et al., 2021; Zhou et al., 2012), which has several limitations: (i) MoCap systems depend upon physical markers attached at anatomical points, limiting the number and density of trackable landmarks; (ii) motions and deformations at unmarked locations are not captured or analyzed, resulting in ignoring the complete surface deformation; (iii) it remains uncertain whether sparse discrete landmarks is adequate for capturing the complex deformation pattern of breast movement. In this research, four-dimensional (4D) scanning technology is introduced to record whole surface deformation information of the breasts, furthering the understanding of the breast deformation patterns from the sparse landmark level to continues surface level.

To support sports bra design, merely recording and analysing breasts deformation patterns are not enough. Previous studies on breast motion have developed biomechanical finite element (FE) models to simulate the interaction between the bra and breasts (Chen et al., 2013; del Palomar et al., 2008; Sun et al., 2019b; Sun et al., 2019c) to provide comprehensive evaluation of the sports bra's performance during different kinds of activities or under different activity intensities. FE modelling has been applied to biomechanics research to predict the pressure and temperature distributions, soft tissue deformations, and the influence of a specific design factor on the overall performance of the sports bra, such as the influence of tightly fitted apparel on body reshaping and comfort sensation (Dan et al., 2011; Wittek et al., 2015; Zhang et al., 2002).

Nevertheless, the application of the FE method in sports bra design is still in its infancy, since proper description, representation, and simulation of the highly complex non-linear attributes of the breast, which inherent from its highly irregular geometry, are still challenging. The accuracy of the constructed FE breasts model greatly depends on the accuracy of the parameterization of the breast material properties, including the viscous damping and hyper-elastic behaviors of the breast tissues, which can diverge

significantly in different breast size, age, and even hormonal status. Due to these difficulties, the mechanical properties of the breasts that are derived from ex-vivo material tests and in-vivo methods significantly vary with invalidated parameters (Eder et al., 2014; Kalra & Lowe, 2016; Ramião et al., 2016).

1.2 Research gaps and objectives

To improve the prediction of the mechanical properties through in vivo behaviors, different experimental techniques has been proposed to determine the material properties of the breasts for constructing subject-specific FE models of the breasts (Doyley, 2012; Han et al., 2011; Sun et al., 2019b). However, comparing with the advances in numerical simulation, the techniques for obtaining input data of the simulation systems, i.e. the capturing, tracking, and analyzing of the complex movement and deformation of the breasts, are relatively lagging behind. In most of the related studies, only static three-dimensional (3D) data are captured by the 3D scanning devices and a limited number of landmarks' movements are captured by the motion capture (MoCap) systems. The limited density of captured landmarks inevitably limits its capability to represent the highly dynamic deformation behaviors of the breasts, therefore inhibiting the accuracy of breasts material properties determination and therefore affected the applicability of the constructed FE model in biomechanics simulations for sports bra design.

To advance the current state of research, suitable devices that can reliably and efficiently capture the higher granularity information of the dynamic breast motion are needed to be adopted. And customized algorithm is needed to be developed for analyzing the obtained information, eventually leading to a better understand of the breast support requirements and advance sports bras designs for optimal breast protection.

To achieve such an objective, the research is separated into 5 parts:

1. To effectively capture the surface changes and stretching of the skin of

the breasts, and changes of the geometry of the breast shape during dynamic motion (walking) by using 4D body scanning technology.

2. To develop Ultra-dense Motion Capture (UdMC) algorithms which can efficiently track specific key points in arbitrary positions to characterize the surface motion and deformation of the soft tissues of the breasts to model the biomechanics of the breasts.

3. To establish a subject-specific FE model for a bra size of 80C to simulate the contact mechanics between a sports bra and the breasts on the basis of the behavior and motion of the breasts.

4. To evaluate the regional deformation and contact pressure of the breasts in response to different bra materials, through FE analyzes and experimental measurements.

5. To compare and validate the breast deformation results of a computational FE model with the experimental results.

1.3 Outline of the thesis

Following the introduction chapter, Chapter 2 provides comprehensive literature reviews on sports bra design, breast biomechanics study, FE model for biomechanics breasts simulation, and the point cloud registration problem.

Chapter 3 presents the application of 4D scanning technology for capturing dynamic breast deformation in vivo with high temporal and spatial resolutions. Based on the data collected data and the `mesh4d` toolkit, a breast anthropometric dataset named *DynaBreastManual* was constructed. In-depth analysis of the in vivo breast deformation patterns were carried out based on this dataset, confirming existing studies on breast deformation patterns as well as extending them to a detailer and clearer presentation of the dynamic characteristics of the breast with 4D scanning data.

In Chapter 4, a semi-automatic method, the UdMC algorithm, is proposed for tracking the complex deformation of breasts during dynamic

activity with a 4D scanning sequence marked with sparse anatomical landmarks. Comprehensive evaluation ot the proposed methods indicates that the UdMC significantly excels the comparison baselines in terms of accuracy, consistency, and efficiency. Two downstream tasks are introduced to demonstrate the practical application of the UdMC algorithm: (i) tracking virtual landmarks in an arbitrary position without attaching physical markers to the region, and (ii) estimating deformation intensity for fine-granularity during dynamic activities.

In Chapter 5, a subject-specific FE biomechanics model of the breast was constructed. For the first time, 4D scanning sequences were introduced as supervision signals for determining subject-specific hyper-elasticity parameters for breasts. Three evaluation metrics were created for optimization: surface-to-surface distance, nodal coordinates deviation and nodal displacement deviation based on the UdMC algorithm. With the optimized material properties for breasts, a bra-breast interaction model was constructed for simulating the ergonomic performance of sports bras made from different materials, leading to critical information previously only obtainable through time-consuming wear trials.

The last chapter, Chapter 6, provides summarization of conclusions derived from the research discussed in this thesis. It also discussed the contributions to the existing knowledge body as well as its limitations. Suggestions on future research directions are thereafter provided.

Chapter 2

Literature Review

2.1 Introduction

Sports bras are anatomically engineered and designed to offer high levels of breast support and physical freedom during physical activities. Inadequate breast support for a long period of time results in discomfort, sagging, pain, and structural damage of the breasts. Physically active women are therefore invariably frustrated in their attempts to find a comfortable and supportive sports bra. To improve the functional design of sports bras, the biomechanical parameters of breast motion and movement are particularly important in the design and development process. Biomechanical studies have confirmed that the breasts move substantially in the vertical, medial-lateral and anterior-posterior directions during treadmill running (Risius et al., 2015; Scurr et al., 2009, 2011; Zhou et al., 2011, 2012). Wearing a suitable sports bra can effectively minimise the amount of breast displacement that occurs during running and/or physical activities. Despite the importance of sports bra design in breast support, technologies that examine the biomechanical aspects of the breasts have been largely absent in the field. analyzes of three-dimensional (3D) body images, breast motion captured by motion capture (MoCap) devices, and computational simulation systems have been used for understanding the complex deformation patterns of the breasts. Nevertheless, these technologies either only provides static images of the breasts surface or only provides limited spatial resolution

information of the breasts' dynamic movements. Due to the lack of comprehensive understanding of the breasts biomechanical properties, sports bras that reduce the breast deformation the most todate have been also perceived to be the most uncomfortable to wear. The current sports bra designs are not sufficiently catering to the needs of active women, thus resulting in a high occurrence of breast pain in many studies.

This chapter reviews studies on the design of sports bras and their breast support performance. The conventional approach of using 3D body scanning systems, MoCap systems and the robust four-dimensional (4D) body scanning approach for analysis of breast motion during dynamic movement of the body are presented. The image processing and registration techniques, as well as biomechanics research of breast support are also comprehensively reviewed.

2.2 Sports bras

Despite the new advancements in breast biomechanics, a dilemma still exists in that a high performance sports bra design can reduce breast movement but results in bra fit problems, discomfort, lack of flexibility in body movement or even health disorders (Coltman et al., 2018). The use of sport bras is significantly restricted by the complex shape geometry and motion behavior of the breasts so that designing a sports bra to reduce the repetitive movement of the breasts during sporting activities with minimal compression is highly challenging (Gefen & Dilmoney, 2007; Haake & Scurr, 2010, 2011). Sports bras are traditionally designed to compress and/or encapsulate the breasts to reduce breast movement, Figure 2.1. Compression sports bras which consist of rigid bra cups uniformly flatten the two breasts together against the chest wall, and tight shoulder straps are usually used. These inevitably induce a high level of pressure to the body, which interferes with breathing, blood circulation and lymph flow with reinforced motion during high intensity exercise. Compared to compression sports bras, encapsulated sports bras which have an underwire, padded cups, and adjustable shoulder straps and underband have proven to reduce breast displacement more

effectively by encasing each breast in a separate structured cup (Yip, 2016). However, due to the lack of information on breast geometry, the breast base and the corresponding design of the underwire are assumed to be semi-circular. Wire related problems for fit, and poor wear sensation and wear comfort are often reported. In a study of 309 women of various breast sizes, 90% of the participants failed the fit assessment of encapsulated style bras (Coltman et al., 2018). Combination sports bras integrate the features of compression and encapsulation bras into one that elevates and supports each breast independently, covered with an external layer of material that compresses the breasts against the chest wall. Breast elevation can reduce tension and loading of the passive anatomical breast support structures, whilst breast compression can decrease the flexion torque generated by the breasts about the thoracic spine. The distance between the centre of the breast mass and the thoracic spine is reduced.

(a) (b)

Figure 2.1: Sports bras: (a) compression bra, and (b) encapsulation bra.

Unfortunately, due to limited biomechanical methods used to quantify complex 3D breast motion, most breast biomechanics research has focused on breast movement during treadmill running and/or women with large sized breasts. Understanding the breast biomechanics and displacements in relation to body position, speed of movement and posture changes during different sporting activities and movements is relatively novel. Typical running activities, short duration of exercise and limited number of participants do not represent the diverse range and at the elite level of sports with different breast support needs in different planes of motion.

Moreover, athletes typically perform high intensity movements over an extended duration of training and competition hours.

Irrespective of the type of bra, suitable bra designs and structural features, together with good fabrication and elasticity behavior are closely linked to control over breast movement, as well as a good fit and comfort. For example, a high neckline can effectively reduce upward breast movement, while adequate tension and elongation of the shoulder straps made of elastic woven tapes can effectively hold a bra in place. Fabric with good stretching and shape retention behaviors can minimise bra displacement during motion. To support the mass of the breasts, support components are a necessity in bra design. The use of cushioning wires and support elements made of plastic and multiple layers of foam, however, not only affects the fit of bras with substantial gapping in the cups due to the extra thickness, but also results in bra displacement (Bowles & Steele, 2013; Bowles et al., 2012; Zhang et al., 2021; Zhou et al., 2013). Inducing excessive amounts of compression and pressure onto the body with the use of rigid materials may lead to internal organ displacement and muscle strain. It is therefore important to control the amount of compression induced by bras and the amount of pressure in bra designs to balance comfort and support. However, to date, there has been very little scientific work that provides accurate and objective techniques to evaluate the impact of various bra features and the types of materials used to avoid breast displacement and provide breast support.

2.3 Current methods in breast biomechanics studies

In terms of biomechanics, breast motion is linked to trunk movement during dynamic movements (Zhou et al., 2011, 2012). When women run on a treadmill without external breast support, the momentum of the movement is transferred from the feet to the torso. The breast and trunk therefore move simultaneously together with a small delay at different moving speeds or activity levels. Biomechanical studies have confirmed that when the trunk

is ascending, the breasts are descending (Zhou et al., 2012). The forces generated from the breast motion are influenced by a number of variables, such as the structure and properties of the soft breast tissues, size of the breasts, internal forces associated with the level, speed and type of activities, etc. (McGhee & Steele, 2020) Women with large breasts experience more breast pain and pressure generated by the bra shoulder straps so that more support is necessary (Coltman et al., 2018; McGhee et al., 2013). They are also subjected to more frictional skin injuries from their bra and have greater difficulties in achieving optimal bra fit. The level of breast support also needs to be increased for older women to compensate for reduced anatomical support due to changes in their breast composition, density and elasticity with aging. The magnitude and frequency of breast motion together with body positioning in different sports have a major influence on the unique breast support requirements for the different planes of motion. More vertical support is required for jumping and horseback riding as compared to cycling and walking (McGhee et al., 2013).

Information on the direction and magnitude of the body and breast movements during various sporting activities helps to identify the amount of breast support needed for an optimal sports bra design. However, due to the complex nature of the soft tissues of the breasts, evaluation methods of the dynamic movement of the breasts and the control requirements of the entire breast during various sports activities are still lacking (McGhee & Steele, 2020).

2.3.1 3D body scanning technology

The use of 3D body scanning technology allows a variety of angles and shapes as well as linear measurements to be reliably and accurately obtained within a few seconds of time. As reported in the product page of 3dMDbody scanning system adopted in this research, the reconstruction error is under 0.7 mm [1]. The 3D scanned body images can be presented in different forms: point, line, surface, shape, and volume. As compared to traditional manual

[1] https://3dmd.com/products/#3dmdbody-system-product-specifications

measurements, 3D scanners are capable of obtaining information on complex body shapes and providing more precise and reproducible data for assessment of bra fit problems (Bowles et al., 2012; Kim & Kang, 2003; Lee et al., 2004; Zhang et al., 2021).

Nevertheless, considering the end-use and range of motion during sporting activities, the extent of body movement during a particular activity must be more accurately quantified when designing sports bras. The amount of body expansion and contraction at skin stretch during sporting activities should also be considered. For example, the changes in the upper body surface measurements between a standard anthropometric position and various active postures such as shoulder flexion, scapula protraction, and scapula elevation have been examined by using a 3D body scanner in previous studies (Chi & Kennon, 2006; Choi & Ashdown, 2011; Lee et al., 2001). Significant changes in body measurements are found, which correspond to the body movement at the joints. However, it is noted that the use of body scanning technology to obtain precise body measurement data during dynamic postures is still challenging as the measurement data could be collected in selected postures. The system merely shows the body surface changes between a static controlled posture and a number of limited static poses (Lee & Ashdoon, 2005). The reproducibility of the measurements is greatly affected by posture differences throughout the scanning process and the quality of the image registration and re-orientation for the evaluation of body and breast movements.

2.3.2 3D motion capture system

The problems of body scanning technologies are resolved by using MoCap systems which allow researchers to measure the changes in the surface of the body over time and during continuous movement (Zhou et al., 2012). As for the accuracy of 3D motion capture systems, as an example, Vicon motion capture system reported a measurement error down to 0.017 mm [2]. Even

[2] https://www.vicon.com/wp-content/uploads/2022/07/Vicon-Metrology-Solutions.pdf

though physical movement and posture changes can be consistently tracked, the results cannot be translated to body surface measurements. The number and placements of body landmarks are vital for motion analyzes while the control of landmarks is always time consuming and troublesome. Hence, many current studies generally use a single reference point on the nipple in relation to the sternal notch to capture the movement of the breasts. However, the breasts consist of non-uniform and soft-tissue masses that are likely to move in complex 3D patterns (Arch et al., 2018; Sohn & Bye, 2014; Zhou et al., 2011, 2012), while the regional displacement of the breasts is substantially different from that of the marker placed over the nipple. With reference to a total of 54 retro-reflective markers (Arch et al., 2018), the magnitude of breast motion in the X, Y and Z directions during treadmill running was measured and analyzed. The results indicated that most of the breast movement occurs above or below the nipple region and at the interface between the bra strap and body.

2.3.3 Computational modelling of human body

More recently, computer modelling such as finite element (FE) simulation has been used to predict the biomechanical interactions between the body and bras. The analysis can be detailed as a body consists of skin, fat tissues, bones, organs, as well as a simple rigid body. The simulation process of breast deformation by using FE modelling is however more challenging and time-consuming since the interactions between the elastic fabric and breasts which are viscoelastic, are highly complex. The ability to simulate the human body and/or breasts strongly depends on the accuracy of the characterisation of the breast properties including the different viscous damping values and hyperelastic behavior of the breast tissues and their continuous changes in properties with breast size, age and even hormonal status (Chen et al., 2013; del Palomar et al., 2008; Domingo et al., 2014; Eder et al., 2014).

2.4 Finite element method for breast biomechanics modeling

2.4.1 Ex-vivo and In-vivo Biomechanical Properties of the Human Breast

FE Model for Modelling Breast Biomechanics Figure 2.2. The tissues and macro- or micro-structure of the breasts directly contribute to their deformation, thus constituting rather complex elastic and viscous properties and behavior. Therefore, accurately determining the material properties of the breast tissues is very important for reliable biomechanical modelling. Various experiments have been conducted for this purpose. There are basically two types: (i) ex-vivo and (ii) in-vivo measurements.

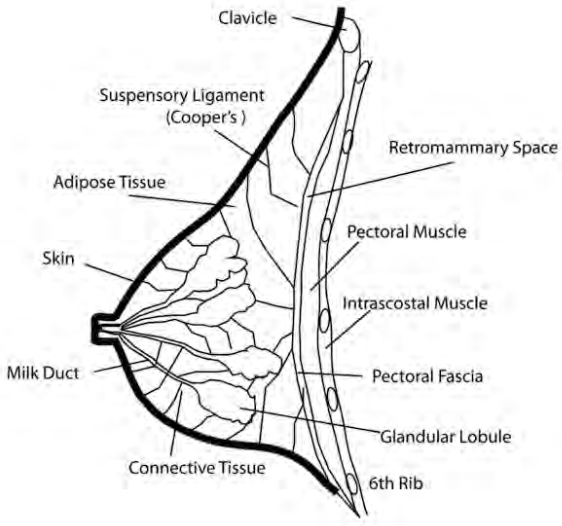

Figure 2.2: Illustration of female breast anatomy illustration (Hipwell et al., 2016).

The measurements of the biomechanics properties of ex-vivo tissues are usually obtained through tension and compression experiments. Uniaxial compression experiments have been conducted on 150 ex-vivo specimens of healthy, cancerous, and fibroadenomatous tissues (source). The results show

that the fibroadenomas are 4 times stiffer than normal tissues, and cancerous tissues are nearly 7 times stiffer than normal tissues (Sarvazyan et al., 1995, pp. 223–240). Stiff breast tissue may point to the risk of breast disease. In term of the biomechanics properties, research has shown that the Young's modulus of normal breast fibroglandular and fat tissues are equivalent; to be specific, around 3 kPa, under small compression. On the other hand, the stiffness of the malignant tumours and high-grade, invasive, ductal carcinoma shows 30% to 60% and 130% increments, respectively (Samani et al., 2003; Samani & Plewes, 2007).

Although the biomechanics properties of ex-vivo breast tissues have been measured in various research, it is generally accepted that among the population and across the life-time of an individual that the mechanical properties of living tissues vary widely (Hipwell et al., 2016). Elasticity imaging techniques that can implement in-vivo measurements have been developed, including sono- and magnetic resonance elastography, shear wave elasticity imaging and mechanical imaging (Parker et al., 2012). The elasticity parameters of in-vivo tissues are estimated by solving the inverse solution based on the detected displacement/strain fields (Doyley, 2012).

2.4.2 Construction of the biomechanics FE model

In computational modelling, the FE method shows a clear, explainable physical picture and is built on a very robust mathematic foundation. From a mathematics point of view, a FE model can be seen as the weak form of a partial differential equation. Reynaldi et al. (2012) showed an example of transforming the intractable differential equation into a clear, lite-weight linear equation. showed an example of transforming an intractable differential equation into a clear, lightweight linear equation. In terms of the importance of differential equations in a wide range of disciplines, FE models have been used with great success in numerical simulation, physical modelling and engineering (Logan, 2012, pp. 2–4).

With all of these advantages, FE modelling is considered to be a very useful method for biomechanics research, including the biomechanical

modelling of the breasts. The mainstream construction of biomechanics FE models is elasticity-based, including hyperelasticity models like the neo-Hookean (Chen et al., 2013) and Mooney-Rivlin (Eder et al., 2014) models. For model parameter estimation, early studies usually adopted the material properties measured from ex-vivo or in-vivo experiments as the initial values, and then manually adjusted them according to the difference between the prediction of the FE model and the experimental results. Nevertheless, manually adjusting the parameters is not only time-consuming but also cannot ensure global optimum parameters. del Palomar et al. (2008) found that with the proportion of each tissue set as its weight, the weighted average of the entire breast can be adopted without losing drastically accuracy. To estimate the proportion, computed tomography (CT) was introduced. Sun et al. (2019b) proposed a systematic parameter method to iteratively estimate the nonlinear Mooney-Rivlin material coefficients.

Other than elasticity-based models, innovative modelling ideas are also available. For example, the heat transfer model is used as an approximation of the mechanical behavior of the breast, since to some extent, the expansion of breast tissues is similar to the diffusion of heat (Unlu et al., 2005). The breasts may also be thought of as fluid with filled fibres so that the fluid mechanism model can be used to approximate the breast behavior (Costa, 2012).

More recently, machine learning (ML) has been introduced to enhance the capabilities of FE models, especially in terms of speed, since the clinical application has very high requirements for real-time processing capability. Martínez-Martínez et al. (2017) used FE modelling to generate simulations for the breasts of 10 subjects, and each simulation required 10 or more steps, which finally summed up to 162 deformations. Then all of these simulations were separated as nodal data and used to train the ML model as a more rapid alternative in lieu of the time-consuming FE simulation. The results showed that amongst the various ML models, extremely randomised trees (ERTs) perform well with the error of most node distances under 2 mm and an average computational time of 0.1 s.

2.5 Problems of 3D data registration in 4D body scanning Technology

The dynamic 4D body scanner uses a novel scanning technology which provides 360-degree full body coverage capturing of a range of poses in 4 dimensions, see Figure 2.3. The scanner is a technical solution for recording high time-resolution 4D data, i.e. a series of 3D data scanned at a specific time interval. The 3D data, in this context, are a form of data that represents the geometric shape and characteristics.

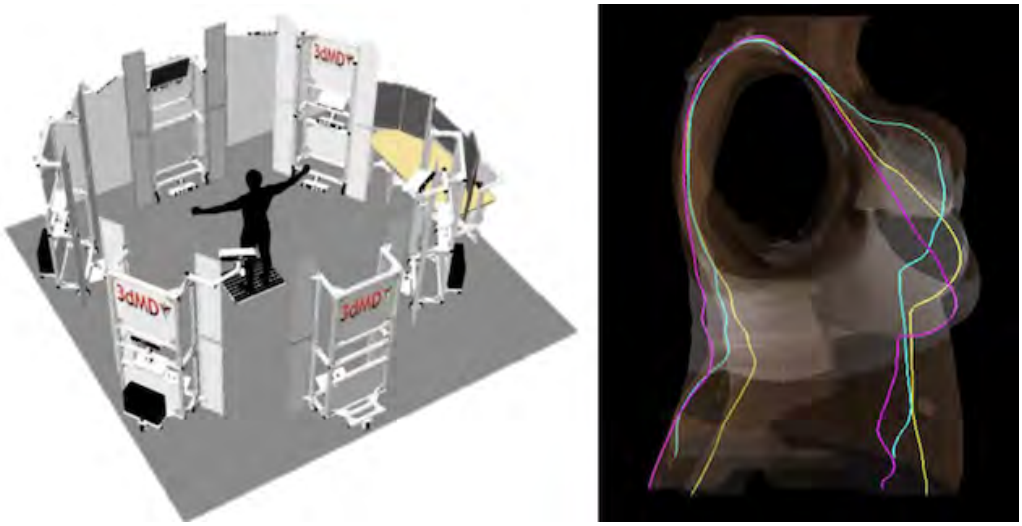

Figure 2.3: 3dMD system setup and contour shapes of breast during motion in sagittal plane.

As indicated by Pei et al. (2021b), the fourth dimension given by 4D scanning technology is particularly crucial in breast motion analyzes. During physical activities, the breasts usually have a time delay in displacement with the torso when the relative displacement of the breasts is determined. Although the displacement of breasts has been extensively examined, conventional 3D body scanning systems merely show the body surface changes between a static controlled posture and a number of limited static poses. Motion capture systems with multiple markers attached onto the body only provide limited spatial resolution and surface geometry information

and a large number of body landmarks for motion analysis are required. The control and placement of markers are time consuming, thus posing technical difficulties for marker identification and tracking of breast motion and changes in breast morphologies. Most breast motion analyzes therefore quantify the movement of the nipples in relation to the sternal notch as a measurement of breast movement. However, this method only provides a gross measure of the overall breast movement. It is apparent that nipple displacement as a measure only provides a gross indication of the overall breast motion in that the non-uniform properties of the soft tissues of the breasts and the complex behavior of the breasts are largely neglected. Four-dimensional scanning technology makes it possible to track the entire breast with movement which offers more information on the changes of breast shape during physical activity.

Nevertheless, with 120 frames taken per second, technical problems can arise in handling and managing a large number of 3D scans or frames. Pei et al. (2021b) only extracted 3 keyframes within a running cycle. The head and the limbs were also manually removed for each of the selected scans. Due to posture changes such as body rotation during motion, registration of the key points from multiple 3D images and point clouds is also challenging and time consuming.

Basically, there are two major types of 3D data: point clouds and meshes. A point cloud is a set of 3D points in space and each point is expressed by a vector that contains the Cartesian coordinates of the point as defined in Equation 2.1. Moreover, a mesh is a structural build of a 3D model that consists of polygons and, of course, each polygon is constructed by a set of linked points. Examples are shown in Figure 2.4.

$$C = \{p_i | p_i = (x_i, y_i, z_i) \in \mathbb{R}^3, i = 1, 2, ..., n\} \tag{2.1}$$

There are various ways to transform a point cloud to a mesh and vice versa. Yuksel (2015) proposed a method of evenly sampling a mesh to a point cloud. The process starts with numerous sampling points and removes points according to the distributed sampling criteria so that eventually desirable

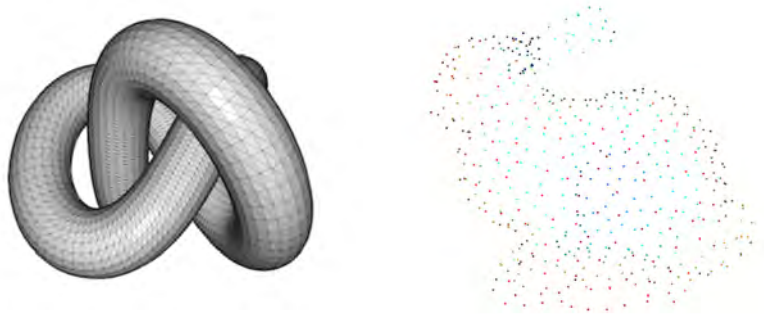

(a) (b)

Figure 2.4: (a) example of a mesh of a complex 3D twisted tube, and (b) example of a point cloud of a bunny.
From Open3D Documentation
http://www.open3d.org/docs/release/tutorial/geometry/mesh.html

samples of point clouds can be obtained. On the contrary, various methods inspired by different geometric perspectives have been proposed to implement an inverse procedure, i.e. surface reconstruction. Edelsbrunner et al. (1983) proposed the alpha shape method to construct mesh from a point cloud based on the alpha shape theory, which is a generalisation of a convex hull, and the resultant mesh consists of caps, arcs, and points. Since the original shape of the object may not fit with the assumed alpha shape, the surface reconstructed by such an algorithm may deviate from the real one. Bernardini et al. (1999) also proposed the ball pivoting algorithm (BPA) which starts with a seed triangle with a ball pivoting around the edges of the triangle but maintains contact with the endpoints of the edges. When the ball touches any 3 points but does not fall through them, a local triangle of the mesh is created. Compared with the alpha shape method, BPA delivers a more refined mesh, even though the entire surface still has bulges and unevenness. To address the problem of surface smoothness, Kazhdan et al. (2006) proposed Poisson surface reconstruction based on solving regularised optimisation problems.

Compared with meshes which consist of partial polygons that are defined by a complex inter-point topological relationship, point clouds are a simpler representation of the geometric structure of a 3D object. Thus, in 3D data

processing, point clouds are a more desired format to contain geometric information. They have become the primary data format to represent the 3D world and various high-resolution sensors like LiDAR and Kinect which are developing rapidly (Huang et al., 2021).

2.5.1 Point cloud registration problems

In 4D body scanning, the dynamic changes of the body are represented by a series of 3D frames; and in this case, 3D point clouds. Therefore, before taking the 3D data for any meaningful analysis of body and breast motion, the first task is to reveal the correspondence between frames (ideally, point-wise corresponding).

Point cloud registration involves many steps that align a number of overlapping point clouds. Typically, a point cloud registration algorithm consists of three components: (i) a transformation model $T_\theta(p)$ over the spatial domains $p, x \in \mathbb{R}^3$, where θ denotes the set of model parameters; (ii) a cost function Ψ to estimate the similarity between the between the deformed frame and the target frame, as defined in Equation 2.2, where the D function is a pure distance estimation function and the λ function is the optional regulation function; and (iii) an optimization strategy $\arg\min_\theta(\Psi)$ to minimise the cost function (Hipwell et al., 2016).

$$\Psi = D(I(T_\theta x), R(x)) + \lambda(T_\theta(x)) \tag{2.2}$$

Once the transformations between frames are revealed, the part of the object in a frame that can be moved to another part in that frame is determined, therefore revealing the correspondence between frames. According to the deformation model type, the registration methods can be roughly classified into two groups (Hipwell et al., 2016):

1. **Rigid Registration**

   Only allows rigid transformation, including rotating, scaling, or affine transformation which are all linear transformations. Thus the transformation model can be expressed by dot multiplying the original

point p_i with a 3×3 transformation matrix; and translating which can be described by adding the original point p_i with a 3×1 vector. For example, the slicing of a box on the conveyor can be regarded as a rigid transformation.

2. **Non-rigid Registration**
   Allows non-rigid transformation, which means that every part of the object can move in different directions and for different distances. For example, the deformation of the soft tissues during activity can be regarded as a non-rigid transformation.

Since this project focuses on the breasts, a typical type of soft tissue complexity, the development of a non-rigid point cloud registration method will be first reviewed in Subsection 2.5.2. The development of rigid point cloud registration, which also has certain application value in this project, will be reviewed in Subsection 2.5.3. Point cloud registration with auxiliary modalities is also an interesting direction towards more reliable and accurate point cloud registration, which will be reviewed in Subsection 2.5.4.

2.5.2 Non-rigid point cloud registration

The difficulty of non-rigid point cloud registration has been described as a *chick-and-egg problem*: the corresponding relationship can be determined if the optimal transformation is known, while on the contrary, the determination of the corresponding relationship, in the first place, needs the optimal transformation (Huang et al., 2021). Non-rigid transformation needs every part of the object to freely deform, but this should not be too free so that there is it is beyond the realm of reality, which is a contradiction. As a result, the core challenges of proposing reliable non-rigid registration are (i) proposing a deformation model and a corresponding optimisation scheme that can well align two frames; and (ii) applying effective regularisation to avoid unrealistic deformation - such as the head in the first frame should not deform itself to the position of the foot in the next frame, although such transformation may align the two frames quite meticulously.

Rueckert et al. (1999) proposed one of the earliest non-rigid point cloud registration methods based on a free-form deformation model defined by a set of control points and using B-splines to produce a smooth varying deformation. The distance between the deformed cloud point and the target point cloud are estimated and the B-spline parameters are then optimized. Applying B-spline deformation to an object is similar to twisting the space according to a control point. The smoothness of B-splines as a geometric property can constrain deformation from creating excessive distortion. This B-spline based method has been widely used in the field of medical image registration, such as MRI-CT registration, PET-CT registration, and registration between breast X-ray images before and after compression (Behrenbruch et al., 2003; Diez et al., 2010; Pinto et al., 2010). An example is shown in Figure 2.5 (Behrenbruch et al., 2003). Note that a key limitation is that when it comes to objects. the movement of different partials are highly independent, such as the legs and arms of a running man.

The Gaussian mixture model (GMM) based registration is another widely used non-rigid cloud point registration method. Various approaches under this method have been proposed to tackle a wide range of non-rigid point cloud registration challenges, including overcoming the effect of noise and outliers (Bishop, 2016; Rasoulian et al., 2012). The Coherent Point Drift (CPD) method proposed in Myronenko et al. (2006) deals with point cloud registration as a probability estimation problem. The point cloud is converted to a Gaussian mixture distribution around the 3D space. The goal of the algorithm is shifting point cloud A to optimize its probability to generate another point cloud B. To apply effective and systematic yield constraint to the deformation, the motion coherence theory (MCT) (Yuille & Grzywacz, 1988; Yuille & Grzywacz, 1989) was introduced, which is based on the assumption that the points close to each other tend to move coherently. By implementing regularization on the displacement (or velocity) field, the transformation is forced to be smooth. Figure 2.6 shows an example of CPD non-rigid registration. Note that 2D cloud points are used because they are more clearer and easier to read on printed pages. In recent years, deep learning enhanced GMM models have been introduced to conduct non-rigid

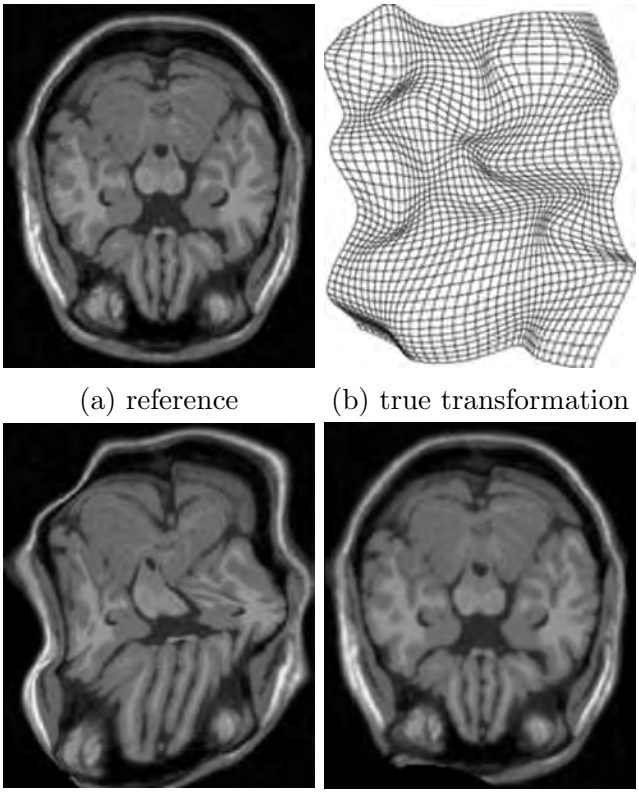

(a) reference (b) true transformation

(c) source (d) result

Figure 2.5: The (a) reference image under (b) transformation generated (c) source image. After B-spline non-rigid registration between (c) source and (a) reference, the untwisted (d) result is recovered (Behrenbruch et al., 2003).

registration tasks, such as DeepGMR which uses a deep neural network to learn the correspondence between points and the GMM components and the GMM parameters can be determined in forward propagation through the network, which increases the speed of parameter optimization and reduces the computational cost (Yuan et al., 2020).

2.5.3 Rigid point cloud registration

Compared with non-rigid registration, rigid registration only allows rigid transformation, including rotating, scaling, affine transformation, and translating (Hipwell et al., 2016), as shown in Figure 2.7. All of these transformations $T_\theta(p)$ can be expressed in:

(a) Noiseless fish point sets registration (91×2 points, $w = 0$);

(b) Registration of 2D fish point set with missing points ($w = 0.5$);

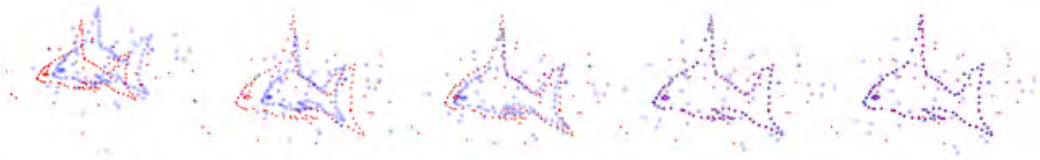

(c) Registration of 2D fish point set in presence of outliers ($w = 0.5$).

Figure 2.6: Non-rigid CPD registration of 2D fish point sets. Initial state and state after 10, 20, 40, and 50 iterations (a to c) (Myronenko et al., 2006).

$$T_\theta(p) = T \cdot p + d \tag{2.3}$$

where p is a point from a source point cloud, T is a 3×3 matrix that can express the linear transformation including rotating, scaling, and affine transformation, and d is the translation from the original position to the target position. More specifically, there are certain constraints to T in different kinds of rigid transformations:

1. **Rotation with Scaling**
   T should be orthogonal, which means that all of the columns of T should be orthogonal with each other, i.e. $t_i^T t_j = 0$ if $i \neq j$, where t_i, t_j denote the i-th and j-th columns of T, respectively. Thus a more concise requirement can be laid out that $T^T T$ should be a diagonal matrix.

2. **Rotation without Scaling**
   T should be unity orthogonal. In addition to the orthogonal

requirement, unity requires that the each column of T should be a unit vector. i.e. $\|t_i\|_2^2 = t_i^T t_i = 1$. Thus a more concise requirement can be laid out that $T^T T = I$.

3. **Affine Transformation**
   T can be any 3×3 matrix, which means that each dimension can be scaled and rotated independently. However, generally speaking, we don't want a transformation that compresses a 3D point cloud into a 2D plane, is not desirable so usually a constraint is added where $\det(T) \neq 0$.

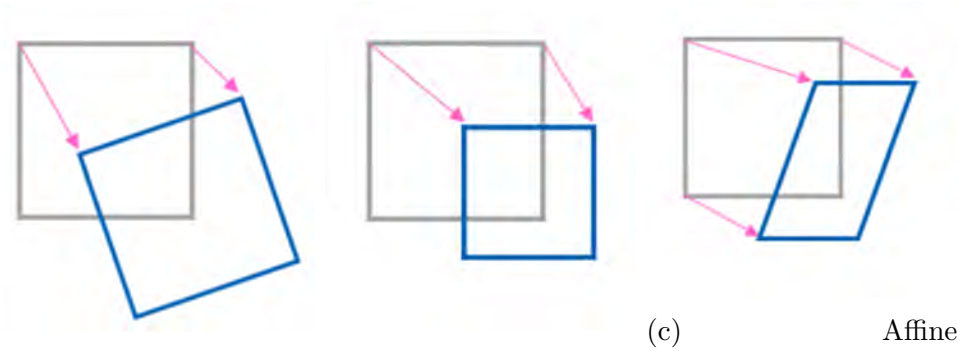

(a) Rotation with translation; (b) Scaling with translation; (c) Affine transformation with translation.

Figure 2.7: Examples of (a) rotation with translation, (b) scaling with translation, and (c) affine transformation. Source: Denis Fedorov https://vicuesoft.com/blog/titles/Affine_Motion/

According to Equation 2.3, there is only a 3×3 matrix and a 3×1 vector is needed to be estimated, i.e. only 12 parameters to determine a rigid transformation. Thus, the realisation of rigid registration is comparatively simpler Besl and McKay (1992) proposed the iterative closest point (ICP) that shows optimized parameters can be identified in an iterative way. Firstly, according to a given initial transformation, finding the closest points correspondence between the transformed source point cloud and the target point cloud are marked. Secondly, with the point-wise correspondence, using the least-squares method is used to estimate new parameters for the transformation. These two steps are implemented repeatedly until the

cost function is minimized to an acceptable level. Apart from estimating point-wise correspondence according to the closest point-to-point distance, some variants use the closest point-to-plane distance as the estimation criterion (Chen & Medioni, 1992; Khoshelham, 2016; Ramalingam & Taguchi, 2013). Other than these variants of ICP, CPD that has been reviewed in can also be used to implement the rigid registration (Myronenko & Song, 2010).

Objects are assumed to only endure rigid transformation in rigid registration. From the perspective of the application, such deformation between different point clouds of the same object is usually introduced by different scanning positions, orientations, and devices. For example, a handheld 3D scanner device can only scan part of an object, thus the 3D point clouds scanned from different perspectives shall be registered so that they can be aligned together to form the entire object (Kleiner et al., 2014; Park et al., 2010a; Park et al., 2010b). An interesting similar application scenario is the map reconstruction for autonomous driving (He et al., 2021; Wang et al., 2019; Zheng et al., 2022).

Pei et al. (2021b) conducted an exploratory study on automatic bust measurements during running by using 4D scanned data. Since the upper torso does not face the front all the time during running, reorientation was carried out on the selected body frames. They tried to automate this task by utilising the positional information of the physical markers. The process was found to be very challenging since the markers easily and frequently went missing. Although the running body is not a rigid object, its deformation is minimal since the time-resolution of the 4D scanning is up to 120 frames per second (fps). Therefore, the body can be approximately considered as a rigid object. Rigid rotation and translation of the human body can then be estimated by using the rigid registration method.

2.5.4 Surface registration with auxiliary modalities

The task of revealing the dense correspondence between surfaces can be particularly challenging when dealing with highly flexible and featureless

surfaces, such as the human breasts. Prior research has attempted to tackle this problem by incorporating information from other modalities (Bogo et al., 2014; Kovnatsky et al., 2013). The Extended Coherent Point Drift (ECPD) method was proposed by Golyanik et al. (2016), which embeds sparse prior correspondence information within the CPD framework to offer additional guidance for registration. Besides directly incorporating prior correspondence, a number of studies have utilized texture information to provide further guidance or rectification for registration (Bogo et al., 2014; Bogo et al., 2017; Gall et al., 2008). Both FAUST (Bogo et al., 2014) and Dynamic FAUST (Bogo et al., 2017) enhance body textures by printing high-frequency patterns onto the subject's skin. This results in more precise and resilient registration compared to methods that solely rely on geometric data (Pons-Moll et al., 2015). However, these techniques require laborious and uncomfortable skin preparation before and after the scanning procedures. Furthermore, due to the lack of ground-truth correspondence data, these methods are assessed based on certain checking criteria (Bogo et al., 2017), which may not sufficiently meet the reliability standards required for breast anatomical and biomechanics research purposes.

2.6 Conclusion

Although plenty of biomechanical studies have been carried out on breast motion analyzes during dynamic motion to optimize the design of sports bras, the amount of breast displacement greatly varies with size, age and level of physical activity of the wearer. Many breast biomechanical research studies are limited by an inadequate research design and biomechanical methods that fail to quantify the complexities of 3D breast motion. More valid and reliable methods that accurately measure the complexities of 3D body and breast motions are necessary to improve the design of sports bras to better support the breasts of women with different physical exercises. With the development of 4D body scanning technology, the 4D data facilitate studies of dense surface deformations and postures. Dynamic anthropometric data can be recorded and systematically analyzed. To do so, an efficient and accurate

approach for 3D data registration is particularly necessary to process and analyze 4D data. This study offers a new scientific approach to advance understanding on breast motion for FE modelling the biomechanics of the breasts. Design features and materials of sports bras can be strategically optimized to better control breast displacement during physical exercise.

Chapter 3
4D Scanning of Breast Deformation In Vivo

3.1 Introduction

The human breasts are complex organs that experience significant deformations during physical exercise and daily activities, potentially leading to discomfort or even harm (Greenbaum et al., 2003). Sports bras have been designed to protect the breast tissues from excessive deformations (Mason et al., 1999; Page & Steele, 1999; Starr et al., 2005), mitigating the bouncing, sagging, and swinging of the breasts during active activities. However, these bras may impose a high level of pressure on the wearer which could lead to negative effects (McGhee & Steele, 2010). Therefore, in order to design sports bras that effectively restrict breast movement while reducing strain on breast tissues, it is crucial to thoroughly understand the dynamic patterns of breast motion and deformation.

With advancements in motion capture (MoCap) technology, various studies have captured and analyzed dynamic behavior of breasts based on anatomical landmarks, confirming their complex three-dimensional (3D) movements due to non-uniform soft-tissue masses (Sohn & Bye, 2014; Zhou et al., 2011, 2012). Nevertheless these studies possess three inherent limitations: (i) MoCap systems depend upon physical markers attached at anatomical points, limiting the number and density of trackable landmarks;

(ii) motions and deformations at unmarked locations are not captured or analyzed, resulting in ignoring the complete surface deformation; (iii) it remains uncertain whether sparse discrete landmarks is adequate for capturing the complex deformation pattern of breast movement.

On the other hand, 3D scanning technology can provide comprehensive surface area data. This technique has been applied in anthropometric studies on human body surface. The primary types of 3D scanning systems include laser-based systems, structure-light systems, as well as multi-view stereo systems (Bartol et al., 2021). All these techniques necessitate subjects maintaining specific static positions during scanning after which the collected signals are used to reconstruct the scanned surfaces. Results are typically exported as mesh data - comprising arrays of vertices, edges, and faces to represent the surface topology. Post-processing, feature extraction, and measurement can subsequently be conducted on the mesh data for extracting geometric information. For example, it can provide accurate and reproducible data assessing bra fit issues(Bowles et al., 2012; Kim & Kang, 2003; Lee et al., 2004; Zhang et al., 2021). Despite offering detailed information of the subtle geometric features, its application is restricted to static postures, thus limiting its applicability on the study of dynamic movement and deformation patterns of the breasts. Some researchers attempted to overcompensate limitation by having the subjects maintain intermediate postures of the activity during scans (Choi & Hong, 2015; Chowdhury et al., 2012; Nasir et al., 2015). However, this approach poses difficulties for the subjects who are required to hold these postures. Furthermore, it may not accurately represent realistic movements in free motion.

Recent advancements in 3D scanning technology have speedup the capture of 3D images to the millisecond level, thereby allowing for continuous scanning of human subjects during dynamic activities. i.e. four-dimensional (4D) scanning (Yang et al., 2020). This technique enhances 3D scanning by incorporating an additional dimension: time. The output of 4D scanning is typically a series of mesh data that represents the scanned surface recorded at different times, as illustrated in Figure 3.1. Commercial systems offering

(a) 0.0s

(b) 0.3s

(c) 0.6s

(d) 1.0s

(e) From left to right are frames of 0.0s, 0.1s, ..., 1.0s.

Figure 3.1: 4D scanning mesh sequence recorded in the experiment.

high scan rates and precision are now accessible, including the 3dMD body scanner (3dMD Ltd., Atlanta, U.S.), capable of performing up to 120 frames per second (fps) with a system error below 0.7mm [1]. The primary focus of this chapter is to introduce the application of 4D scanning technology for capturing dynamic breast deformation in vivo with high temporal and spatial resolutions. A breast anthropometric dataset namely *DynaBreastManual* was constructed, which stimulating in-depth analysis of breast deformation

[1] https://3dmd.com/products/#3dmdbody-system-product-specifications

patterns as well as further studies in the following chapters.

It should be noted that parts of this chapter are derived from a submitted manuscript titled *An exploratory semi-automatic approach for dense tracking of breast motion in 4D.*

3.2 Construction of *DynaBreastManual* dataset

3.2.1 Data acquisition

In order to capture real-time data on the dynamic deformation of the breasts during active movement, a female participant of age 31, height 168 cm, weight 65 kg, and breast size 80C was recruited for dynamic 4D body scanning. Prior to her participation in the study, informed consent was secured in writing. The experiment received ethical clearance from The Hong Kong Polytechnic University Ethics Committee (HSEAR20210305003). To construct the motion model by recording anatomical landmarks, 26 pearl hard base markers were attached around breast-related anatomical landmarks that could be captured by optical cameras and aligned as texture of the reconstructed meshes. This method is more time-efficient and easier to clean up after scanning compared to Dynamic FAUST (Bogo et al., 2017), which involves painting features onto skin. Moreover, it allows precise marking of anatomical landmark positions.

3.2.2 4D scanning and landmarks labelling

A 3dMD body scanner (3dMD Ltd., Atlanta, U.S.) equipped with 30 optical cameras surrounding the scanning area was utilized for capturing images from various angles and reconstructing a dynamic surface mesh of human surface based on multi-view stereo. The subject performed 6km/h fast walking in braless condition on a treadmill while being scanned at the scanning rate of 120 fps - the maximum scanning rate offered by the system. A 121 frames

sub-sequence comprising approximately one gait cycle was selected for further analysis.

The selected meshes were then imported into `mesh4d`, a software package developed during this research for 4D data processing [2]. It was observed that holes/breaches were occasional appeared in lower areas of the breasts due to insufficient camera coverage towards these perspectives. For better visibility and image quality considerations, only 18 out of 26 markers were selected as shown in Figure 3.2. The selection of anatomical landmarks is based on previous research on breast biomechanics (Sun et al., 2019a; Zhou et al., 2012) and their anatomical descriptions are summarized in Table 3.1. These landmarks are grouped into the *clavicle, right breast, left breast, and rib cage bottom* areas for further analysis.

During the landmark labeling stages, the frame sequence were divided into adjacent chunks each containing 12 frames covering 100 ms per chunk. Landmarks coordinates of the first frame of each chunk were manually labeled, while those of the subsequent frames were estimated using quadratic interpolation. Given the high sampling rate of manual labeling, these estimated coordinates should have ground-truth accuracy.

Utilizing these accurately labeled landmark coordinates, a lightweight dynamic 4D human breast anthropometric dataset was created and named *DynaBreastManual* [3]. This dataset comprises 18 anthropometric landmarks across 121 frames of reconstructed 3D scenes - totaling up to 2178 ground-truth landmark coordinates. The data instances in this set follow a specific referencing convention: the i-th frame's mesh matrix is denoted as $V_{body}^{(i)} \in \mathbb{R}^{3\times N^{(i)}}$, where column $v_j^{(i)}$ represents the three-dimensional coordinates for vertex j, with superscript indicating frame index. Similarly, attached landmarks for this particular frame are represented by landmark matrix $C^{(i)} \in \mathbb{R}^{3\times K}$; here column $c_k^{(i)}$ denotes three-dimensional coordinates for landmark k, with subscript indicating landmark index and superscript representing frame index. It should be noted that corresponding landmarks

[2]The source code can be accessed via GitHub: https://github.com/liu-qilong/mesh4d.

[3]The dataset can be accessed via https://github.com/liu-qilong/udmc. Please note that due to privacy considerations, mesh texture has been withheld.

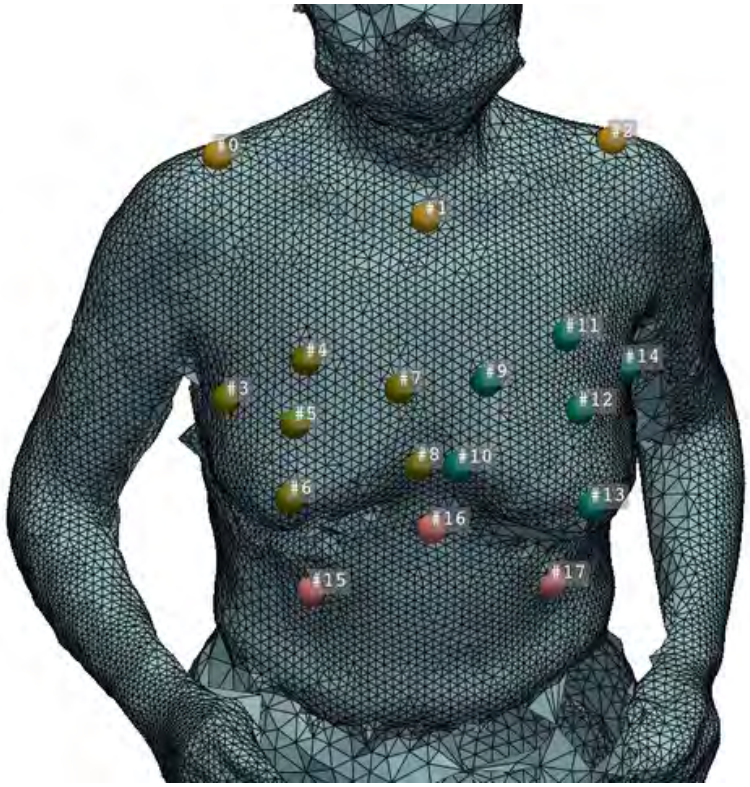

Figure 3.2: The labelled anatomical landmarks. Landmarks on the clavicle, left breast, right breast, and rib cage bottom regions are represented as yellow, green, blue, and pink lines, respectively.

across different frames share identical indices, i.e. the landmark $c_k^{(i)}$ is directly corresponding to $c_k^{(i+1)}$ in the next frame.

3.2.3 Automatic breast cropping scheme

The breast area was automatically cropped out based on the contour landmarks of the breasts:

Approach. Automatic breast cropping

1. For the i-th frame of the mesh, the landmarks $c_0^{(i)}, c_2^{(i)}, c_3^{(i)}, c_{14}^{(i)}, c_{15}^{(i)}, c_{17}^{(i)}$ are selected as breast area contour. The landmark indices is combined as a set $K = \{0, 2, 3, 14, 15, 17\}$

Table 3.1: Anatomical descriptions (ISO 8559-1:2017 (2017)) of the labelled landmarks. The selection of anatomical landmarks are based on (Sun et al., 2019a; Zhou et al., 2012).

Index	Description	Region
0	Acromion of the left shoulder	
1	Front neck point	Clavicle
2	Acromion of the right shoulder	
3	Breast outermost point	
4	Upper breast point over the right nipple	
5	Middle breast point over the right nipple	Right breast
6	Nipple point of the right breast	
7	Right cleavage dot	
8	Breast innermost point	
9	Left cleavage dot	
10	Breast innermost point	
11	Upper breast point over the left nipple	Left breast
12	Middle breast point over the left nipple	
13	Nipple point of the left breast	
14	Breast outermost point	
15	Beneath the right breast	
16	The front processus xiphoideus	Rib cage bottom
17	Beneath the left breast	

2. Upper bound cropping
   Calculate the maximum height h_{max} of all contour landmarks, crop out the mesh part under the level plane at height $h_{max} + \psi$, where ψ is an adjustable factor for slightly enlarging the cropping area. Appropriate ψ is empirically selected as 30 mm.

3. Lower bound cropping
   Calculate the minimum height h_{min} of all contour landmarks, crop out the mesh part above the level plane at height $h_{min} - \psi$.

4. Estimate the approximate breast plane based on the contour landmarks:

(a) The center point of all contour landmarks $c_o^{(i)} = \frac{1}{6}\sum_{k\in K} c_k^{(i)}$ is regarded as one point on the breast plane.

(b) In an ideal scenario, all contour landmarks are on the breast plane. In this case, the normal vector n of the plane should be perpendicular to $(c_k^{(i)} - c_o^{(i)})$, which forms 4 linear equations $(c_k^{(i)} - c_o^{(i)})^T n, k \in K$.

(c) To exclude 0 vector from the solution space, an extra linear equation $\|n\|_1 = 1$ is added.

(d) In practical scenarios, the contour landmarks may not coplane. Therefore, the 5 linear equations are solved with least-square method [4]and then rescale the solution as a unit vector, adopted as the optimized estimation of the norm vector $\hat{n}$. Together with point $c_o^{(i)}$, the breast plane is defined.

(e) For the sake of geometric completeness, the point $c_o^{(i)}$ is slightly moved towards the inverse direction of the norm vector $\hat{n}$: $\hat{c}_o = c_o^{(i)} - \psi\hat{n}$. With $\hat{c}_o, \hat{n}$, the breast plane is estimated.

5. Crop the body mesh with the approximate breast plane and removed all disconnected parts. Then the breast area of the mesh is extracted from the body mesh.

The i-th frame of the cropped out breast is denoted as mesh matrix $V_{breast}^{(i)} \in \mathbb{R}^{3\times N^{(i)}}$. The automatically cropped out breast areas are shown in Figure 3.3.

3.3 Result

With the coordinates of the anthropometric landmarks labelled from the 4D scanning sequence, different aspects of the dynamic patterns including the overall trajectories, accumulated regional displacement, and deformation intensity distribution can be analyzed. The statistical results based on the

[4]The implementation of the least-square method is based on `NumPy` (Harris et al., 2020).

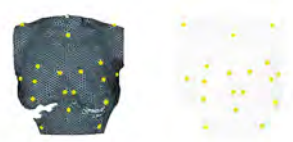

(a) 0s

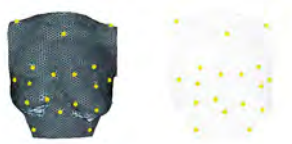

(b) 1/3 s

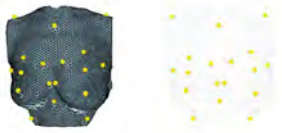

(c) 2/3 s

(d) 1 s

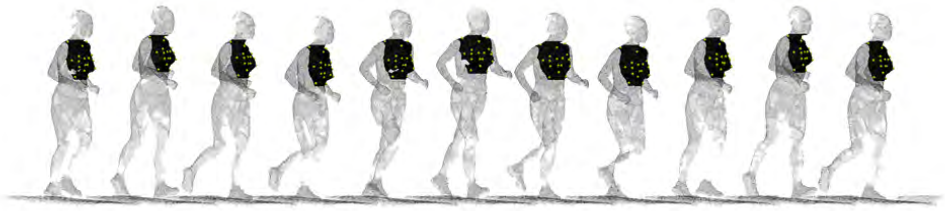

(e) From left to right are frames of 0.0s, 0.1s, ..., 1.0s.

Figure 3.3: Breast area cropped out based on contour landmarks.

sparse landmark trajectories can be interpolated and projected onto the automatically cropped breast areas (Figure 3.3), thus providing a detailer and clearer illustration of the dynamic breast deformation pattern as compared with previous works (Zhou et al., 2012).

3.3.1 Overall movement of anthropometric landmarks

As shown in Figure 3.4, the variation of landmarks coordinates of z-axis (caused by forward and backward movements) is significantly less than

those of x-axis (caused by lateral movements) and y-axis (caused by vertical movements), indicating that the vertical and lateral swinging are the primary movements trends of the breasts during fast walking. Figure 3.5a shows the frame-wise coordinates curve of different landmarks, illustrating a coherent movement trends in x-axis and y-axis but incoherent movement trend in z-axis. By separating the z-axis curves according to the region of the landmark, as shown in Figure 3.5b, we found that the incoherency of landmarks movement in z-axis originates in the opposite movement trends of the left and right breast areas - due to the swinging movement during fast walking.

To prominently illustrate the overall movement of the landmarks, the spatial trajectories of different landmarks are shown in Figure 3.6. These trajectories constitute a butterfly-like spatial pattern which is consistent with previous research on breast movement patterns (Zhou et al., 2012), thus confirming that the highly dynamic and complex nature of breast soft-tissue deformation patterns.

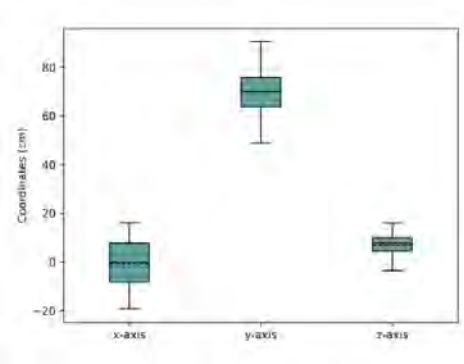

Figure 3.4: Coordinates distribution of 17 body landmarks in x, y and z axis.

3.3.2 Accumulated displacement of anthropometric landmarks

Figure 3.7a and Figure 3.7b show the accumulated trajectory length of different landmarks and the accumulated trajectory length of different

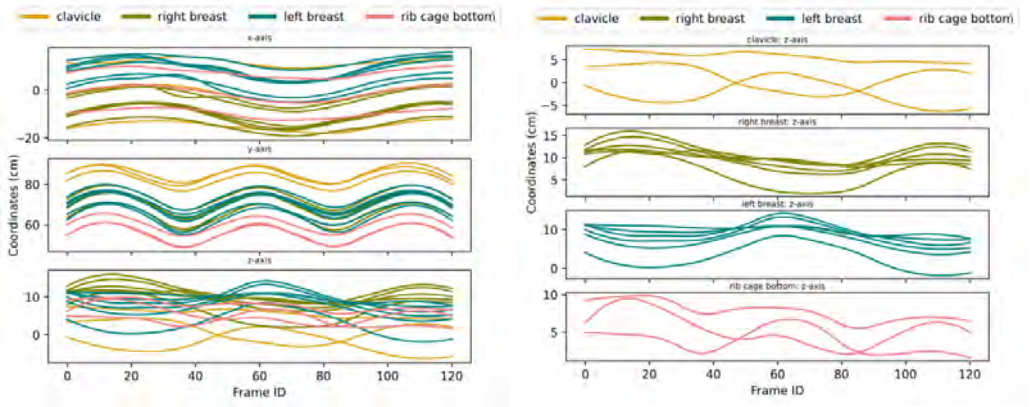

(a) (b)

Figure 3.5: Regional motion in anterior-posterior direction throughout the 121 frames: (a) x, y, z-axis curves with all landmarks plot together; (b) z-axis curves with landmarks from different regions plotted separately.

landmarks across frames, respectively. The results show that the accumulated trajectory lengths of the different landmarks range from 50 cm to 80 cm, which is a significant deformation considering the fact that all of the landmarks are recorded from nearly 1 second of recording. On the other hand, the longest trajectory (Landmark 13) is 48.6% longer than the shortest trajectory (Landmark 0) within the same recording period, thus confirming highly nonlinear deformation patterns of the breasts during dynamic motion.

3.3.3 Deformation intensity distribution

The accumulated displacement can be regarded as an indicator of deformation intensity. In Figure 3.8, sparse landmark accumulated displacements are interpolated and mapped to the continuous breast surface based on the Thin Plate Spline (TPS) interpolation (Duchon, 1977), illustrating the deformation intensity distribution over the breast surface. Two characteristics of the breast deformation patterns can be observed: (i) the deformation intensity increases smoothly from the chest to nipple areas, and (ii) soft tissues are significantly more deformable than the rigid torso

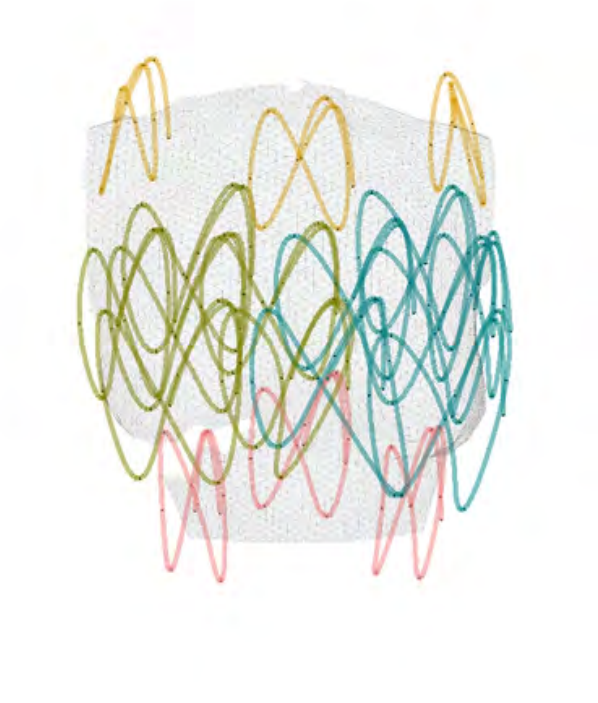

Figure 3.6: Spatial trajectories of different landmarks. Landmarks on the clavicle, left breast, right breast, and rib cage bottom regions are represented as yellow, green, blue, and pink lines, respectively.

areas. These patterns are consistent with the previous research on breast deformation patterns (Pei et al., 2020).

3.3.4 Directional deformation distribution

Other than the overall deformation, the directional analysis of the breast deformation is also interesting because it provides insightful information for sports bra design. To illustrate the directional deformation patterns of the breasts, landmark trajectories were projected to the x, y, and z-axies and the accumulated displacements were calculated accordingly. The sparse landmark accumulated displacements in different axes were interpolated and mapped them onto the continuous breast surface using TPS interpolation, as shown in Figure 3.9. The results present different deformation patterns

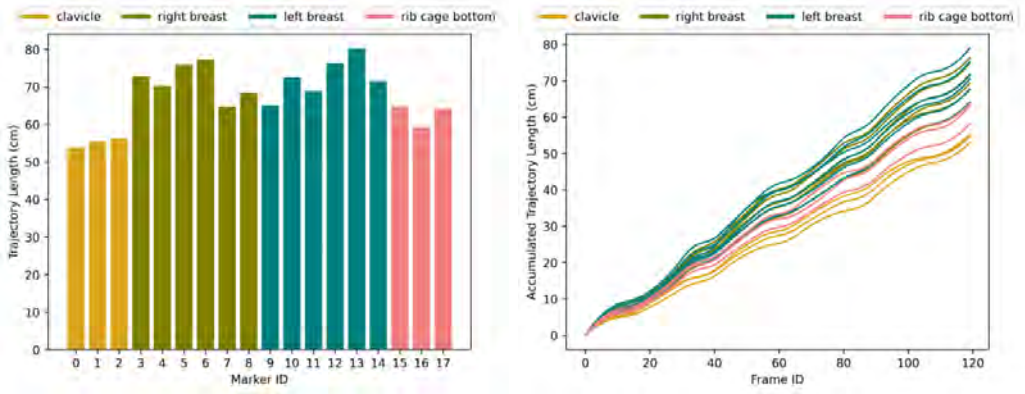

(a) (b)

Figure 3.7: Accumulated trajectory length: (a) accumulated trajectory length of different landmarks; (b) accumulated trajectory length of different landmarks across frames.

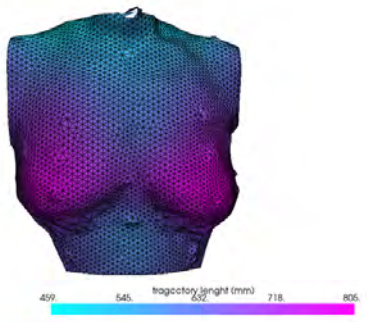

Figure 3.8: Accumulated displacement distribution of the surface skin at torso.

in various directions: the entire breast area and the chest area is subjected to large medial-lateral deformations (x-axis), while only the soft tissues of the breasts are subjected to obvious vertical deformation (y-axis). Both the lateral and vertical deformations are more pronounced on the front side of the body. In contrast, significant deformations in the forward and backward directions are observed on the side-parts of the torso. These observations may inspire sports bra designs with better support features like reinforced sections or more appropriate textile materials to better control breast displacement.

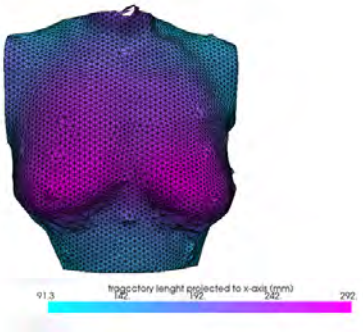

(a) x-axis

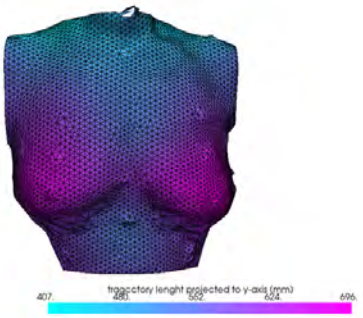

(b) y-axis

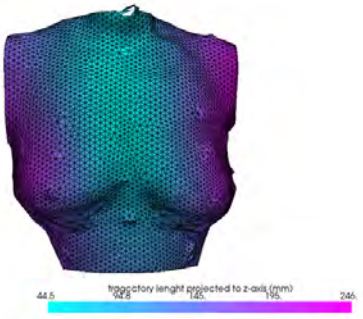

(c) z-axis

Figure 3.9: Directional displacement distribution of the whole breast area.

3.4 Conclusion

This chapter presents the application of 4D scanning technology for capturing dynamic breast deformation in vivo with high temporal and spatial resolutions. The experiment is conducted with a female subject while fast walking, and demonstrates the practicality and effectiveness of this approach.

For processing the 4D scanning sequence, a toolkit named `mesh4d` was developed in this research work, which offers features from landmark labeling to automatic breast area cropping. This tool was instrumental in processing the data captured through 4D scanning.

Based on the collected data and the `mesh4d` toolkit, a breast anthropometric dataset named *DynaBreastManual* was constructed. In-depth analysis of the in vivo breast deformation patterns were carried out based on this dataset, confirming existing studies on breast deformation patterns as well as extending them to a detailer and clearer presentation of the dynamic characteristics of the breast with 4D scanning data.

Overall, these findings emphasize not only the potential but also the versatility of 4D scanning technology in studying dynamic body deformations. Compared with previous works on breast dynamic deformation patterns based on MoCap (Sohn & Bye, 2014; Zhou et al., 2011, 2012), the recording and analyzing of the breast dynamic behavior was advanced from sparse landmarks level to the continues surface levels, providing much higher granularity data for breast anthropometric measurements and analysis. Future research can build upon these results by increasing the sample size or exploring other physical activities to further enrich current understanding on human body dynamics.

Chapter 4

Dense Tracking of Dynamic Breast Deformation

4.1 Introduction

Highly accurate commercial systems with rapid scanning capabilities are now accessible, an example being the 3dMD body scanner (3dMD Ltd., Atlanta, U.S.). This system can scan at a rate of up to 120 fps and has an error margin of less than 0.7 mm [1]. Such precision is sufficient for capturing subtle deformation in breasts, and several studies have already started to leverage this rich data source (Al-Anezi et al., 2013; den Herrewegen et al., 2014; Novak et al., 2014). However, despite advancements in four-dimensional (4D) data collection technology, two significant challenges persist related to data processing: (i) the absence of automated processes. Given that the scanning rate can reach up to 120 frames per second (fps) (or 7200 frames per minute), manually processing such vast amounts of generated data to extract crucial anthropometric measurements is not feasible. Current research typically only extracts a handful of frames from each scan for analysis (Pei et al., 2020, 2021a; Pei et al., 2021b; Zhang et al., 2023), which results in loss of nuanced information on the dynamic procedures and undermines the potential benefits offered by high-speed scanning, and (ii) the lack of a precise and consistent method to show the dense correspondence between

[1] https://3dmd.com/products/#3dmdbody-system-product-specifications

different frames. Although adjacent frames correspond with one another - meaning that one frame of human body mesh deforms into the next - it remains unclear how vertex points within these individual frames correspond exactly. This gap in understanding poses difficulties when attempting to develop automated methods for processing 4D data like tracking anatomical landmark trajectories during dynamic activities.

In this research work, a semi-automatic approach named Ultra-dense Motion Capture (UdMC) is proposed to address the research gap. This method uncovers the dense correspondence between vertices/points across different frames by enhancing sparse, manually-labelled landmarks to serve as initial dense correspondence and subsequently refining the correspondence through an advanced post-alignment scheme. To the best of my knowledge, this is the first systematic procedure designed for the dense tracking of breast motion based on 4D scanned data of an entire surface, which holds considerable promise for studies related to breast biomechanics, anthropometry and ergonomics.

It should be noted that parts of this chapter are derived from a submitted manuscript titled *An exploratory semi-automatic approach for dense tracking of breast motion in 4D.*

4.2 Ultra-dense motion capture algorithm

4.2.1 Mesh morphing and post-alignment

In order to realistically establish a dense correspondence between different mesh frames, each frame of the breast mesh is transformed into the subsequent one. This transformation is based on the Thin Plate Spline (TPS) motion model guided by landmarks and a post-alignment scheme Figure 4.1. Note that in the following sections, the math notation follows the convention that is described in Section 3.2.

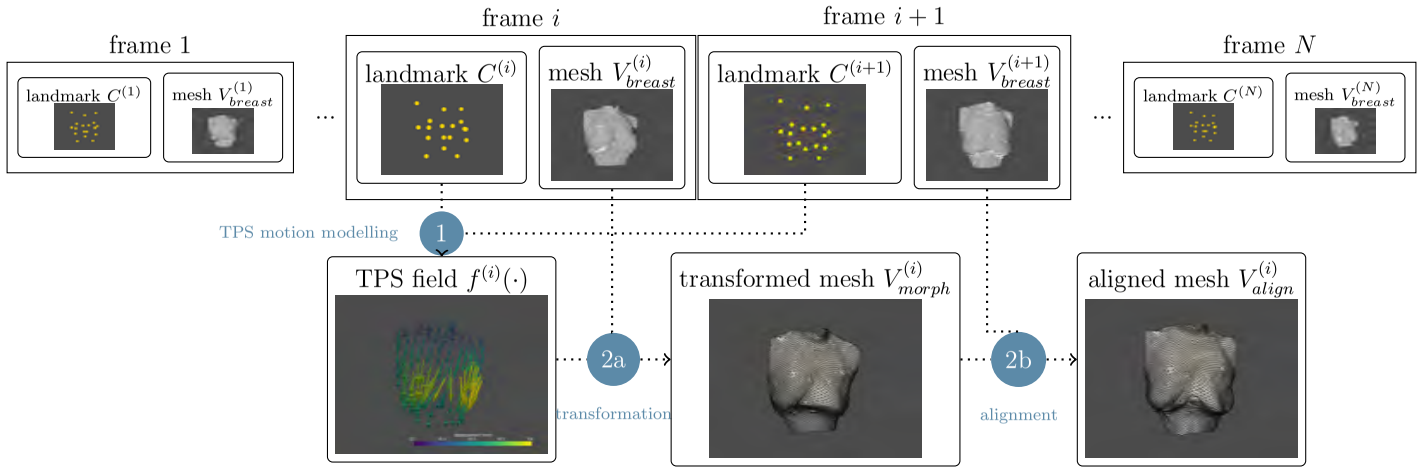

Figure 4.1: Flowchart of the mesh morphing and post-alignment process. It consists of two major steps: (1) TPS motion modelling based on sparse anatomical landmarks, and (2) post-aligning the transformed mesh to the sophisticated 4D scanned geometry. In step (2), there are two sub-steps: (2a) source mesh transformation and (2b) alignment to the target mesh, which results in an aligned displacement field.

(a) TPS motion model based on sparse landmarks

The TPS kernel, a variant of the radial basis function (RBF), is frequently used to interpolate continuous high-dimensional fields from a limited set of control point/value pairs (Duchon, 1977). The derivation of TPS stems from the physical analogy of bending a thin metal sheet and provides several advantages. First, the derivation of TPS can generate an infinitely differentiable field of smooth values. Secondly, its energy function has a physical interpretation. Lastly, manual adjustment of the free parameters is not needed. Owing to these merits, TPS has found extensive use in estimating and characterizing non-rigid transformations (Yang, 2011; Ying et al., 2016). As such, the TPS kernel is used in building the motion model in this study.

The TPS motion model is constructed by using the sparsely labelled landmarks $c_k^{(i)}, k = 1, 2, ..., K$ in the i-th frame as the control points and their corresponding landmarks in the subsequent frame $c_k^{(i+1)}, k = 1, 2, ..., K$ as the value points. These form a set of control point - value point pairs. This motion model allows for determining the coordinates of an arbitrary point in the next mesh frame:

$$\hat{x}^{(i+1)} = f^{(i)}(x^{(i)}) = a_0 + a^T x^{(i)} + \sum_{k=1}^{K} \omega_i \phi(\|x^{(i)} - c_k^{(i)}\|_2) \tag{4.1}$$

where a_0, a, $\omega_i, i = 1, ...K$, represent the coefficients of the TPS model; $\|\cdot\|_2$ denotes the Euclidean norm; and the function $\phi(\cdot)$ represents a pre-defined kernel function with $\phi(r) = r^2 \log r$. The coefficients are solved under constraints that when inputting landmarks $c_k^{(i)}$, their corresponding values should be outputted as $c_k^{(i+1)}$ [2].

Utilizing the established $f(\cdot)$, every column of V_{breast} is transformed to its estimated corresponding coordinates in the subsequent mesh frame, thus yielding a mesh matrix $V_{morph}^{(i)}$.

[2]Implementation of TPS model and its solution is based on `SciPy` (Virtanen et al., 2020)

(b) Post-alignment with the target mesh

Despite the fact that the TPS motion model $f^{(i)}(\cdot)$ can capture the overall movement pattern of the breasts based on identified anatomical landmarks, the model merely provides a rough estimate that depends on the sparse landmarks and may fail to offer well-granularity dynamic characteristics of the breast. To incorporate higher granularity dynamic breasts information into this motion model, 4D scanning sequences for post-alignment are introduced: each column of $V_{morph}^{(i)}$ is further aligned with the target mesh $V_{breast}^{(i+1)}$, where each column from $V_{morph}^{(i)}$ is substituted by using its closest point from the target mesh with a point-to-plane search (Sullivan & Kaszynski, 2019), culminating in an aligned mesh matrix denoted as $V_{align}^{(i)}$.

4.2.2 Full-field mapping of continuous dense correspondence

The dense correspondence between the i-th and $(i+1)$-th frames of the mesh is established by using the mesh matrices $V_{breast}^{(i)}$ and $V_{align}^{(i)}$. However, this only provides correspondence with discrete vertices/points. To construct a full-field map of continuous dense correspondence, TPS (Duchon, 1977) is used for transformation, as follows:

$$\hat{x}^{(i+1)} = F^{(i)}(x^{(i)}) = a_0 + a^T x^{(i)} + \sum_{j=1}^{M} \omega_i \phi(\|x^{(i)} - v_j^{(i)}\|_2) \tag{4.2}$$

where $v_j^{(i)}, j = 1, 2, ..., M$ is the M nearest points of x from V_{breast} and $\|\cdot\|_2$ denotes the Euclidean norm. Given that point movement should be coherent and smooth, it is reasonable to interpolate the motion of any given point based on its neighboring points from within this set. The coefficients (a_0, a, ω_i, where i ranges from 1 through K) are determined by solving with the constraints derived from the corresponding pairs; each pair forms one linear equation. This local interpolation scheme proves more efficient than utilizing all of the corresponding pairs in both sets for mapping.

At this stage, we have constructed a function that maps an arbitrary

point denoted as $x^{(i)}$ in frame i to its equivalent position in frame $i+1$ is constructed, which is denoted as $\hat{x}^{(i+1)}$. The revelation of such dense correspondence across the 4D scanning sequence facilitates a systematic analysis of the dynamic characteristics of the breasts. Two basic downstream tasks are illustrated in the following sections to show its application value.

(a) Virtual landmarks tracking

Traditional MoCap technology relies on physical markers attached directly onto the human body which limits the density of landmarks used for analysis purposes (Section 3.1). With the UdMC, however, dense movements on the anatomical landmarks without physical markers can be tracked based on the dense-correspondence information between frames:

Approach. Virtual landmarks tracking

1. Select a virtual landmark $p^{(1)}$ from the first frame of breast $V^{(1)}_{breast}$.
2. Use the dense-correspondence mapping $F^{(1)}(\cdot)$ to estimate its corresponding point $\hat{p}^{(2)}$ in the 2-nd frame of the mesh.
3. With $\hat{p}^{(2)}$, estimate its corresponding point $\hat{p}^{(3)}$ in the 3-rd frame of mesh in the same way, and so on.

(b) Deformation intensity analysis

The deformation intensity of the breasts is related to discomfort and adverse symptoms (McGhee & Steele, 2010). Understanding the degree of deformation intensity based on different factors can provide insights into the dynamic characteristics as well as inspire designers to design more comfortable bras. To measure the deformation intensity, as in Chapter 3, the trajectory lengths of the anatomical landmarks on the surface of the breast is used as an indicator. Using the results of virtual landmark tracking, the deformation intensity can be determined at fine granularity:

Approach. Deformation intensity analysis

1. Evenly sample V^1_{breast} as 100 virtual landmarks with quadric decimation (Garland & Heckbert, 1997).
2. Track the trajectory of these virtual landmarks and calculate the trajectory length as a metric for measuring deformation intensity.
3. Coloring each surface-partial as a visual illustration of the estimated deformation intensity.

4.3 Result

4.3.1 Construction of comparison baselines

As discussed in Chapter 2, probabilistic methods for surface registration such as the Coherent Point Drift (CPD) algorithm (Myronenko & Song, 2010), produce relatively more reliable and precise outcomes. The CPD along with its recent variants, the Bayesian Coherent Point Drift (BCPD) algorithm (Hirose, 2021), are therefore selected as comparison baselines for geometry-only registration. The Extended Coherent Point Drift (ECPD) registration algorithm (Golyanik et al., 2016) is also chosen as a baseline due to its similarity to the work in this study in terms of introducing prior correspondence [3]. However, texture-based methods like FAUST (Bogo et al., 2014) and Dynamic FAUST (Bogo et al., 2017) are not considered for the comparison baselines since the pattern of the texture is not changed by painting the skin of the subject.

These baselines are used to replace mesh morphing and post-alignment (Subsection 4.2.1) in the approach in this study to construct the comparison baselines. Moreover, given that the computation time for the CPD, BCPD, and EPCD algorithms increases significantly with an increase in the number of vertices, the breast meshes were sub-sampled to 1000 vertices by using

[3]The implementation of the CPD, BCPD, and EPCD algorithms is based on the `probreg` package (Kenta-Tanaka, 2019)

quadric decimation (Garland & Heckbert, 1997) [4]. UdMC alongside the comparison baselines were implemented on a MacBook Air (M1, 2020) (Apple Ltd., California, U.S.) with Python 3.9.16. To assess the performance at varying temporal resolutions and sequence lengths of 4D data, 3 versions of the datasets at frame rates of 10 fps, 60 fps, and 120 fps were created by loading one frame from every chunk of 12 frames, 2 frames, and 1 frame respectively from *DynaBreastManual*. The sub-datasets are referred to as DBL-10, DBL-60, and DBL-120, respectively. The code along with the dataset can be accessed at https://github.com/liu-qilong/udmc.

The quantitative evaluation metrics of all of the approaches for each sub-dataset are summarized in Table 4.1. The results indicate that UdMC significantly excels all comparison baselines across all sub-datasets. A comprehensive description and analysis will be provided in the following sections of this thesis.

Table 4.1: Quantitative evaluation metrics

Dataset	Metric	UdMC	ECPD	CPD	BCPD
DBL-10	time (s)	**0.49**	20.62	17.84	84.88
	acc-c (cm)	**0.11**	0.75	–	–
	acc-nc (cm)	**0.91**	6.11	2.96	4.05
DBL-60	time (s)	**3.19**	108.66	120.60	639.47
	acc-c (cm)	**0.37**	0.68	–	–
	acc-nc (cm)	**0.78**	5.32	7.64	2.67
DBL-120	time (s)	**5.62**	230.22	254.51	1270.08
	acc-c (cm)	**0.43**	0.71	–	–
	acc-nc (cm)	**0.78**	7.24	9.55	3.18

The metrics are dumped for clarity: *time* refers to computation time, *acc-c* refers to alignment error on control landmarks, and *acc-nc* refers to alignment error on non-control landmarks. Note that the *acc-nc* metric is not appropriate for the CPD and BCPD algorithms since they do not use prior correspondence information during the registration procedure.

[4] `PyVista` (Sullivan & Kaszynski, 2019) was used for implementing the quadric decimation

4.3.2 Quantitative estimation

(a) Computation time

The computation time was evaluated during mesh morphing and post-alignment, with consideration of data loading, the pre-processing stages, and downstream task implementation are the same across all methods. As depicted in Table 4.1 and Figure 4.2, the UdMC algorithm consistently requires significantly less computation time across all of the sub-datasets which range from 10 fps to 120 fps (sequence length of 11 to 121), with recorded times being 0.49s for DBL-10, 3.19s for DBL-60, and 5.62s for DBL-120. This result shows that the UdMC algorithm is a more viable and efficient option for breast biomechanical studies, ergonomic research as well as clinical applications.

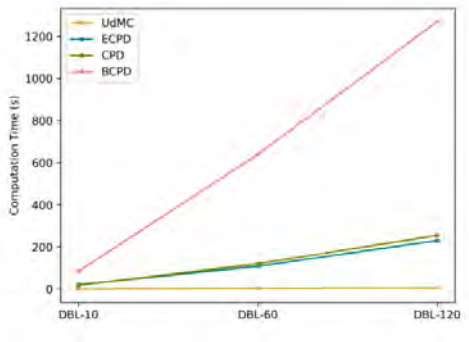

Figure 4.2: Computation time on all frames of *DynaBreastManual*.

(b) Alignment of control landmarks

Both the ECPD and UdMC algorithms use prior-corresponding landmarks (control landmarks) to enhance the estimation of dense correspondence over frames. To assess their performance in following prior correspondences, alignment estimation with virtual landmark tracking was carried out as follows:

Approach. Alignment evaluation on control landmarks

1. Implement virtual landmark tracking based on initial positions of control landmarks from the first frame of data.
2. Compared trajectories of virtual landmarks with ground-truth control landmark trajectories.
3. Estimated average error (deviation from ground truth) and the standard deviation (SD) of the error.

As illustrated in Table 4.1 and Figure 4.3, the UdMC algorithm shows the lowest alignment error across all sub-datasets. The plotted alignment error for each frame suggests that the UdMC aligns the control landmarks more precisely throughout all of the frames, which demonstrates the reliability and consistency of the UdMC in accurate alignments.

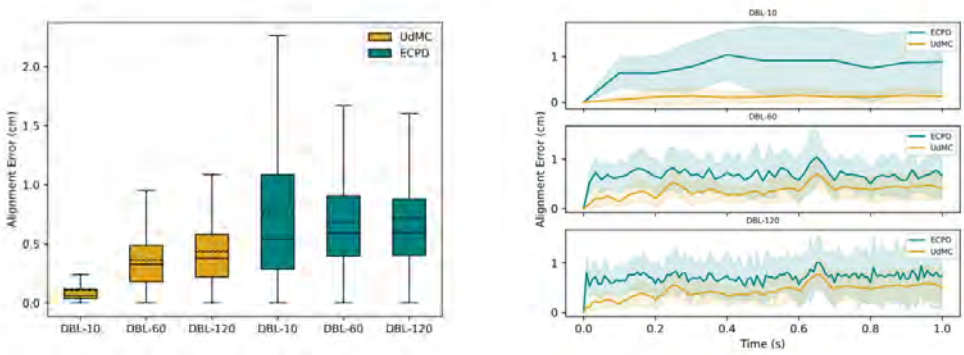

(a) (b)

Figure 4.3: Alignment error on control landmarks. (a) Box plot of overall alignment error: upper/lower boundary of the box represents the third/first quartile of the alignment error; solid/dotted middle line represents the mean/median error; the whiskers extend the box by 1.5 IQR; (b) frame-wise alignment error curve. The solid line represents the mean error of that timestamp, while the shaded region denotes one standard deviation above and below the mean, illustrating variability in alignment errors over time. Noted that CPD and BCPD are neglected from comparison because they don't utilize prior-correspondence information.

(c) Generalization to non-control landmarks

The motion model of the UdMC is established based on the control landmarks, which provides specific ground-truth corresponding points to guide the alignment process. In this case, it is not surprising that the UdMC algorithm provides a good alignment for these particular points. However, the real value of algorithms is in their ability to reveal dense-correspondence on non-control points, i.e. the arbitrary anatomical landmarks on the breast. Therefore, it is crucial to assess the accuracy of the alignment of the non-control points, i.e. the algorithm's capability to generalize to non-control landmarks. To quantitatively determine this accuracy, *leave-one-out validation* was implemented on all of the landmarks, as follows:

Approach. Alignment evaluation on non-control landmarks

1. For registration methods that utilize prior-correspondence information (UdMC and ECPD):
   (a) Each landmark c_k is excluded one at a time from the dense correspondence estimation procedure.
   (b) Implement virtual landmark tracking on c_k, and compared the tracking result with the ground-truth trajectory of c_k. Estimated average error (deviation from ground truth) and the standard deviation (SD) of the error.
   (c) Since c_k was not included in the dense correspondence estimation procedure, we regarded its estimated error as a sample of non-control landmark tracking accuracy.
2. For registration methods that only use geometric information (CPD and BCPD):
   Since these algorithms do not incorporate control points into their dense correspondence estimation, the differences between the results of the virtual landmark tracking for the labelled landmarks

and their actual trajectories can be regarded as an estimation of the accuracy of the non-control points.

The UdMC consistently surpasses the other baseline models by a significant margin according to Table 4.1 and Figure 4.4. When the frame rate increases from 10 fps to 120 fps (sequence length extends from 11 to 121 frames), there is noticeable deterioration in the performance of the CPD algorithm while the performance of the ECPD and BCPD algorithms fluctuates at about their original level. Only the UdMC demonstrates continuous improvement under these conditions, thus indicating its superior scalability with higher frame rates and longer 4D sequences – a vital factor for practical applications. In addition to the overall alignment errors, it is also critical to examine the plotted alignment errors for each frame since they reflect the consistency of the method across frames due to cumulative tracking errors. As illustrated in Figure 4.4b, the errors of the CPD, ECPD, and BCPD algorithms rapidly accumulate over successive frames whereas the UdMC has both few errors and a stable performance throughout the entire process, which suggest that the method in this study is more reliable and robust for tracking breast motion.

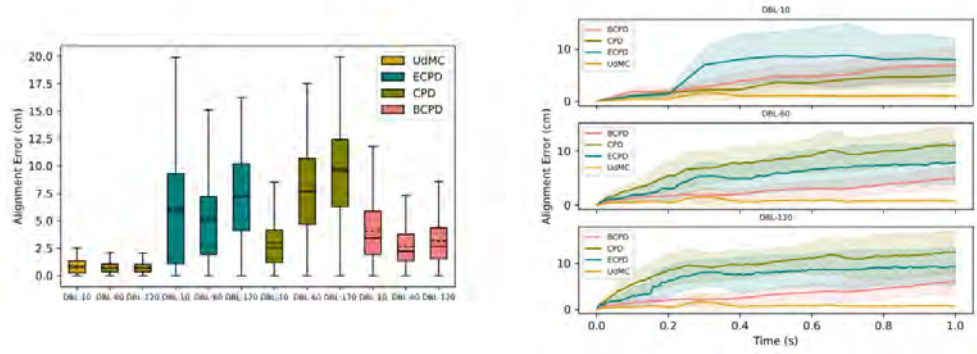

(a) (b)

Figure 4.4: Alignment error on non-control landmarks. (a) Box plot of overall alignment error; (b) frame-wise alignment error curve. Plotting configuration follows Figure 4.3;

4.3.3 Qualitative estimation on downstream tasks

The qualitative assessment of the performance of all the methodologies on the downstream tasks is presented in Subsection 4.2.2.

(a) Virtual landmarks tracking

To demonstrate the efficacy of tracking the virtual landmarks, 5 random points from the initial frame of a mesh were chosen as the virtual landmarks. Their trajectories were then tracked in the subsequent frames, as depicted in Figure 4.5. The videos of the tracking results for all of the methods can be found at https://github.com/liu-qilong/udmc.

Note that these virtual landmarks are chosen solely for their visual lucidity. Under the hood, every point on the surface of the breast can be densely tracked based on the full-field mapping of continuous dense correspondence outlined in Subsection 4.2.2. The results indicate that the UdMC successfully aligns the points trajectories to the swinging motion of the breasts while the ECPD algorithm causes distorted points layout during the latter half of the breast movement. The CPD algorithm also tends to allocate all of the points towards the bottom, whereas the BCPD algorithm tends to cluster all of the points together.

To show the overall pattern of the breast movement captured by each algorithm, the continuous trajectory of each virtual landmark is plotted as shown in Figure 4.6. While the ECPD and BCPD algorithms create unordered and overlapping trajectories (particularly at higher frame rates and longer sequences), the UdMC and BCPD show smooth butterfly-like patterns consistent with previous research on breast movement patterns (Zhou et al., 2012). However, it was observed earlier that the BCPD requires a significantly longer calculation time and tends to cluster all of the landmarks together which introduces severe artifacts into the estimated trajectories. These observations suggest that only the proposed approach in this study effectively and accurately captures the complex dynamics of breast motion.

DBL-10

(a) UdMC (b) ECPD

(c) CPD (d) BCPD

DBL-60

(e) UdMC (f) ECPD

(g) CPD (h) BCPD

DBL-120

(i) UdMC (j) ECPD

(k) CPD (l) BCPD

Figure 4.5: Virtual landmarks tracking results of UdMC and baselines. For each plot, from left to right are frames of 0.0s, 0.1s, ..., 1.0s.

DBL-10

(a) UdMC (b) ECPD (c) CPD (d) BCPD

DBL-60

(e) UdMC (f) ECPD (g) CPD (h) BCPD

DBL-120

(i) UdMC (j) ECPD (k) CPD (l) BCPD

Figure 4.6: Tracked trajectory of the virtual landmarks.

(b) Deformation intensity illustration

Deformation intensity graphs were generated by using all of the algorithms. As shown in Figure 4.7, the ECPD algorithm fails to provide a smooth and consistent deformation pattern while the CPD and BCPD show a gradual increase in the deformation intensity from the chest area towards the nipple areas but do not distinguish between the deformations that occur within the breast and the rib cage area beneath the breast. In contrast, the UdMC algorithm identifies variations between the soft tissue deformations within the breast compared to the comparatively rigid rib cage areas. This aligns with the breast deformation patterns observed in Pei et al. (2020) on 4D mesh sequences. These results indicate that the UdMC algorithm provides a more accurate measurement of the intensity of the breast deformation.

4.4 Conclusion

In this chapter, a semi-automatic method, the UdMC algorithm, is proposed for tracking the complex deformation of breasts during dynamic activity with a 4D scanning sequence marked with sparse anatomical landmarks. *DynaBreastManual*, a dynamic 4D anthropometric dataset of the human breasts constructed in the research as discussed in Chapter 3, is used to benchmark the UdMC along with 3 other baseline methods adapted from previous studies. The results indicate that the UdMC significantly excels the comparison baselines in terms of accuracy, consistency, and efficiency. For the complete 120 fps dataset, average errors of 0.43 cm for the control-landmarks and 0.78 cm for the non-control (arbitrary) points are found at calculation speeds between 40-200 times faster than the other methods.

Two downstream tasks are introduced to demonstrate the practical application of the UdMC algorithm: (i) tracking virtual landmarks in an arbitrary position without attaching physical markers to the region, and (ii) estimating deformation intensity for fine-granularity during dynamic activities. The qualitative assessment reveals that only the UdMC can provide realistic outcomes. To confirm the applicability of the proposed

DBL-10

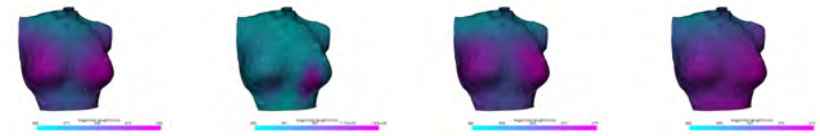

(a) UdMC (b) ECPD (c) CPD (d) BCPD

DBL-60

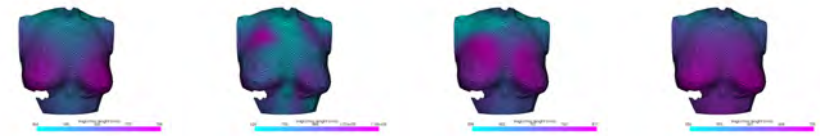

(e) UdMC (f) ECPD (g) CPD (h) BCPD

DBL-120

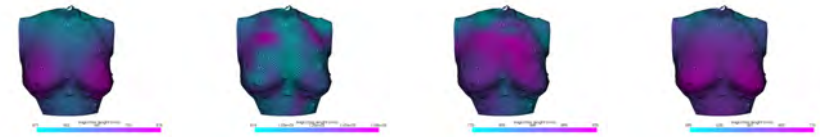

(i) UdMC (j) ECPD (k) CPD (l) BCPD

Figure 4.7: Breast deformation intensity illustration.

method across different frame rates and sequence lengths, evaluations are also conducted on datasets with frame rates of 10 fps and 60 fps where consistent improvements in performance are observed.

The significantly enhanced performance suggests that using 4D scanning sequences with landmarks is a promising strategy for developing a motion model of the surface of the body. This further highlights the potential to advance anthropometry studies at the sparse-landmark level to dense-surface level, thus enabling more comprehensive analyses and understanding of the dynamic deformation patterns and properties of breasts.

Chapter 5
4D Fine-tuned FE Virtual Breast for Sports Bra Design

5.1 Introduction

In previous chapters, four-dimensional (4D) scanning sequences of in vivo breast deformation obtained during treadmill fast walking at a speed of 6 km/h have been systematically analyzed (Chapter 3) and the dense displacement profile of the entire breasts surface was constructed thereafter (Chapter 4), based on the *DynaBreastManual* dataset and the proposed Ultra-dense Motion Capture (UdMC) algorithm during this research. These works have paved the way towards systematic and comprehensive analyses of the patterns of the dynamic deformation of the breasts, which leverage the capability of a 4D scanning system to continuously scan dynamic surface with high temporal and spatial resolutions. Nevertheless, merely observing the dynamic patterns presented in a scanning trial is not the end goal. The soft tissues of the breasts can behave in a highly diverged ways during different kinds of activities or under different activity intensities. Conducting scanning trials that cover all circumstances of interest can be very time-consuming and resource-demanding. Therefore, the transformation from observations of the scanned data to the ability to accurately predict the dynamic behavior of the breasts under different circumstances is crucial for breast biomechanical research as well as facilitating better sports bra designs.

The finite element (FE) method is a well-known approach grounded on solid mathematical foundations. The FE method is used to simulate real-world physical systems, including simulating the soft tissues that higly deformable for research and clinical purposes (Khaniki et al., 2023). With proper construction and application of the boundary conditions, a FE model of the breast can simulate the biomechanical response of the soft tissues of the breasts, such as displacement (del Palomar et al., 2008) and pressure (Sun et al., 2021), under different physical activities and conditions with reasonable accuracy. For example, del Palomar et al. (2008) reported a mean deviation of 2.4 mm between the simulated and ground-truth human body surface and Sun et al. (2019b) reported the root mean square error (RMSE) for a nipple point distance of 0.33% during forward leaning. Aside from simulating the biomechanical response of the breasts itself, the constructed breast model can be further assembled with an FE model of a sports bra or other wearable products, which have tremendous application value in virtual try-on systems and sports wear design validation and optimization (Sun et al., 2019a; Sun et al., 2019c).

A critical challenge in realistically simulating the breast biomechanics is modeling and parameterization of the highly nonlinear hyper-elastic characteristics. A number of strain energy density models have been well developed to describe the hyper-elasticity of materials, including neo-Hookean, Mooney-Rivlin, Ogden, etc. (Khaniki et al., 2023). However, the dynamic characteristics of soft tissues can vary drastically accross the population so it can be very challenging to configure the strain energy density model with the proper parameters for a subject-specif simulation. Traditionally, breast material parameters have been obtained via ex-vivo material tests on small adipose and glandular samples (Samani et al., 2003; Samani & Plewes, 2007). However, these approaches require the intrusive extraction of human tissue samples and the parameters measured on ex-vivo non-bioactive tissue may not provide reliable results. Han et al. (2003) developed a technique to estimate the in-vivo material parameters based on ultrasonic scanning, which only reflects the elasticity. Nevertheless, hyper-elasticity is vital for modelling breast tissue, especially during large

deformation.

To accurately parameterize the subject-specific material properties, various researchers have investigated the approach of the iterative determination of material parameters based on the deviation between the simulation results and the ground-truth data. Sun et al. (2019b) utilized a MoCap system to record the trajectories of the left and right nipple points of a female subject during forward leaning. The FE model was used to predict the distance between the nipple points and thereby compared with the ground-truth data. Optimal material parameters were obtained after 7 rounds of golden section search (GSS) iterations and a 9 segments fine-tuning. The resulting subject-specific parameters were shrunk by a factor of 7.25, which is a significant change, thus confirming the need for the subject-specific setting of breast material parameters. Since these approaches rely on external observations (e.g. landmark trajectories) to fine-tune the material parameters, the capability of the external observations to represent the dynamic characteristics of the soft tissues is crucial for optimizing the material parameters accurately and reliably. However, in Sun et al. (2019b)'s work, only the distance between 2 landmarks (the left and right nipple points) was used as the optimization supervision signal, which may not be sufficient for capturing the complex surface deformation information of the highly deformable soft tissues of the breasts.

Figure 5.1 shows the overall workflow of this chapter. The 4D scanning sequence with high temporal and spatial resolutions information of the entire surface of the breasts will be introduced to determine the subject-specific Mooney-Rivlin material parameters. Based on the dense dynamic displacement profile obtained via the UdMC algorithm as discussed in Chapter 4, surface-to-surface distance, nodal coordinates deviation, and nodal displacement deviation are constructed as the evaluation metrics, which would provide supervision signals with high granularity. To the best of my knowledge, this is the first approach that introduces sophisticated dynamic deformation information for the entire surface from the 4D scanning data to determine the material properties for construction of the subject-specific breast biomechanics simulation system.

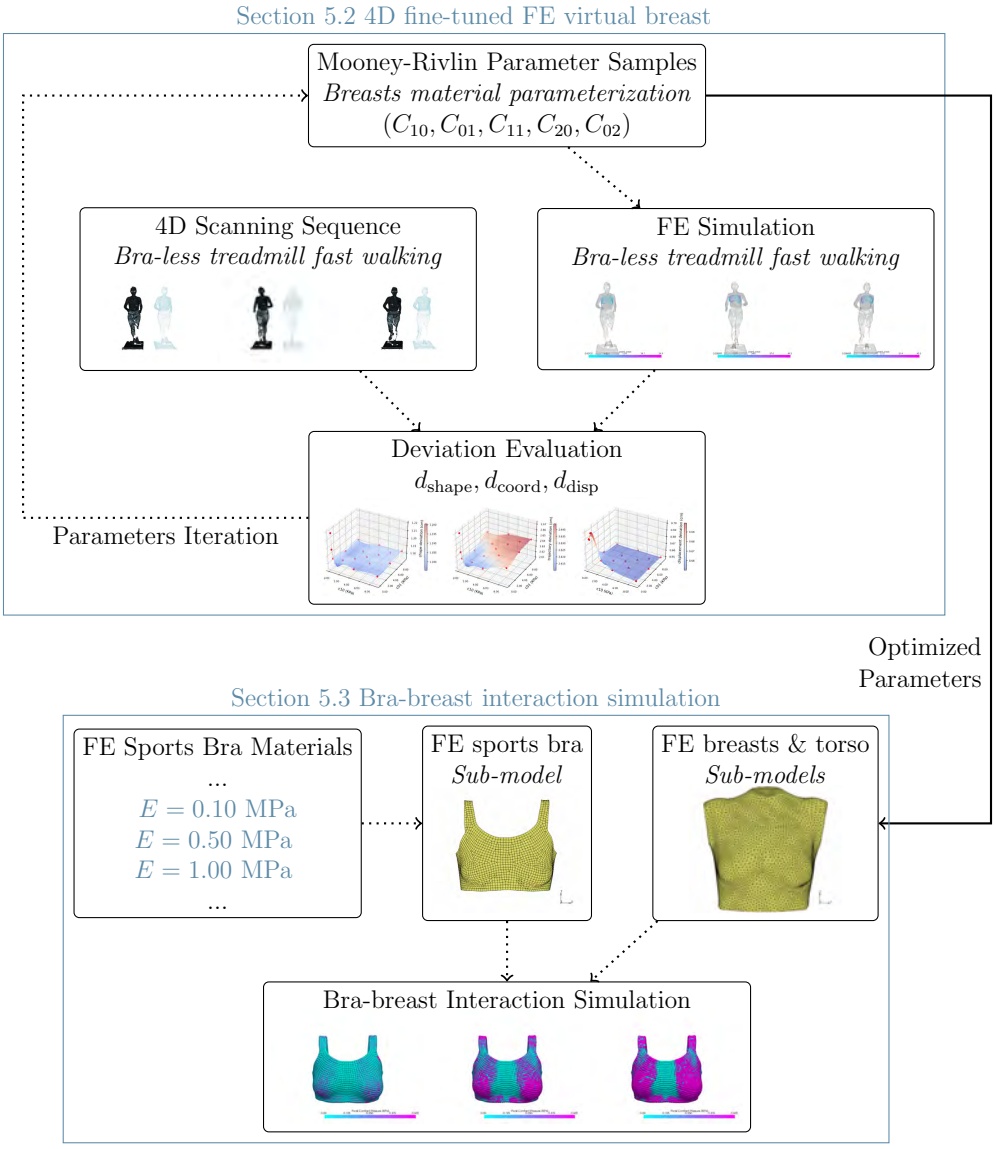

Figure 5.1: Flowchart of Chapter 5.

5.2 4D fine-tuned FE virtual breast

5.2.1 Construction of subject-specific FE model

(a) Parameterization of material properties of the breast

To represent the nonlinear hyper-elasticity of the breast for realistic simulation, a Mooney-Rivlin model was adopted for parameterizing the breast material. To represent the hyper-elasticity of a material, the relationship between stress and strain can be described by using the stress-strain density function (Sun et al., 2019b):

$$W(I_1, I_2) = \sum_{i,j=0}^{n} C_{ij}(I_1 - 3)^i (I_2 - 3)^j \tag{5.1}$$

where C_{ij} are the adjustable material parameters that characterize the nonlinear hyper-elastic material property and I_1, I_2 are the first and second invariants of the Cauchy-Green deformation tensor B:

$$I_1 = \mathrm{tr}(B) \tag{5.2}$$

$$I_2 = \frac{1}{2}[\mathrm{tr}(B)^2 - \mathrm{tr}(B^2)] \tag{5.3}$$

where $B = F \cdot F^T$ and F denotes the deformation gradient.

When $n = 2$, the model is referred to as a Mooney-Rivlin material model with 5 adjustable parameters $p = (C_{10}, C_{01}, C_{11}, C_{20}, C_{02})$. The initial values of the parameters were adopted from the ex-vivo material test of the breast in Samani and Plewes (2004):

$$p^{\text{origin}} = (0.30, 0.31, 2.25, 4.72, 3.80)(\text{kPa}) \tag{5.4}$$

(b) Construction of FE model of the female subject

During the 4D scanning experiment discussed in Chapter 4, aside from scanning during treadmill fast walking, the female subject was also scanned during static standing to acquire a geometric model of the body in the

static state. One frame of the reconstructed mesh of the body was imported into software (Geomagic Studio 12, USA) for refinement, rectification, and meshing. The meshed body was segmented into the torso, the peripheral torso soft tissue, and the breasts soft tissue parts to construct the FE model, as shown in Figure 5.3. Finite element types of the torso part and the breast part were summarizedd in Table 5.1.

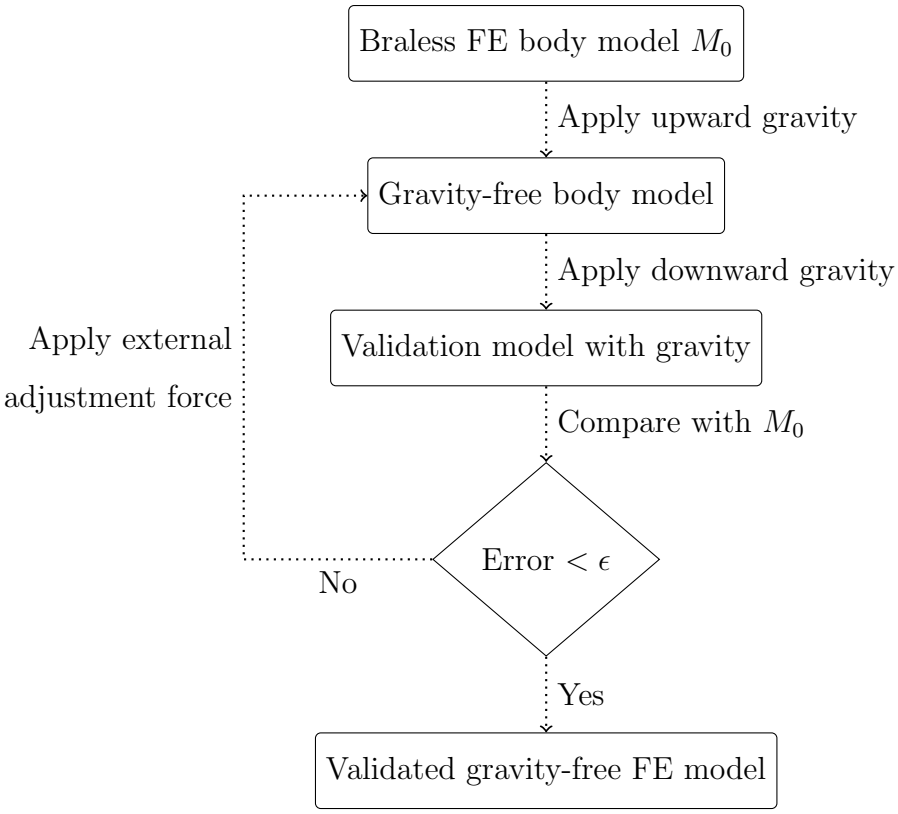

Figure 5.2: Flowchart of iterative gravity compensation scheme to obtain gravity-free FE model.

Table 5.1: Element types of the sub-models of the FE virtual breasts

FE Sub-model	Body Type	Mesh Type	Mesh Size
Breasts soft tissue	Deformable body	Tetrahedron	8 mm
Peripheral torso soft tissue	Deformable body	Tetrahedron	8 mm
Rigid torso	Rigid body	–	–

(a) (b) (c)

Figure 5.3: Subject-specific FE model of the female subject: (a) breast sub-model, (b) soft tissue around breasts sub-model, and (c) rigid torso sub-model.

Then the iteratively compensation scheme shown in Figure 5.2 (Sun et al., 2019c) was implemented on the FE model to obtain the gravity free FE model for FE further simulation.

(c) Boundary conditions obtained from 4D scanning sequence

MSC Marc (Hexagon Ltd. Stockholm, Sweden) was used as the FE analysis solver. To simulate breast deformation during fast walking, two loadcases were applied to the FE model sequentially:

Loadcases. Breast deformation during fast walking

1. Apply gravity force on the gravity-free FE model.
   This load case is simulated as *static analysis*.

2. Apply displacement to the torso part.
   The displacement data was obtained from the landmark 1 from the *DynaBreastManual* dataset constructed in Chapter 3. Noted that the contact type of the breast soft tissue and the torso part are set as *glued interaction* so that the displacement of torso part will thereby initiate the displacement and deformation of the breast tissue. Total increment steps are set as 200 and each step contains a time interval of 5 ms, simulating totally 1s of fast walking as

compatible with the 4D scanning sequence. This load case is simulated as *dynamic analysis*.

5.2.2 Evaluation metrics derived from 4D scanning sequence

To evaluate the accuracy of the simulation results, a 4D scanning sequence was introduced to construct 3 evaluation metrics. A loss function of the parameter optimization process was then constructed based on these 3 evaluation metrics [1]. All of the functionalities related to 4D data processing described in the following sections are provided by the 4D data processing package `mesh4d` developed during this research: https://github.com/liu-qilong/mesh4d.

(a) Data preprocessing

Considering that the FE simulation results consist of inner nodes while the 4D scanning sequence only consists of the surface nodes of the scanned body, the surface nodes of the FE simulation results should be first extracted for further comparison. The node indexes of the surface nodes of the FE sub-model of the breast was extracted for further analysis. Moreover, since the frame rates of FE simulation (200 fps) and the 4D scanning sequence (120 fps) are different, the nodal trajectories of the FE simulation results were firstly interpolated and reframed as 120 fps based on the linear RBF interpolation.

(b) Surface-to-surface distance

Surface-to-surface distance is the most direct estimation of the deviation between the simulated dynamic breast behavior and the ground-truth data:

Approach. Surface-to-surface distance evaluation

1. Frame-wise surface-to-surface distance estimation.

[1] For implementation details, please refer to the evaluation code: https://github.com/liu-qilong/code2023-fe-virtual-breast/blob/main/asset/eval.py.

(a) For j-th node $n_j^{(i)}$ the i-th frame of the simulated trajectories, the nearest point $m_j^{(i)}$ from the corresponding 4D scanning mesh is obtained by nearest point-to-plane search.

(b) Surface-to-surface distance of the i-th frame of the simulated results is defined as the averaged distance between the nodes and their nearest point from the 4D scanning mesh: $d_{\text{shape}}^{(i)} = \frac{1}{N_{\text{node}}} \sum_j^{N_{\text{node}}} \|n_j^{(i)} - m_j^{(i)}\|_2$, where N_{node} is the total nodes number and $\|\cdot\|_2$ denotes the Euclidean distance.

2. The overall surface-to-surface distance is estimated as the average surface-to-surface distances of different frames:

$$d_{\text{shape}} = \frac{1}{N_{\text{frame}}} \sum_{i=1}^{N_{\text{frame}}} d_{\text{shape}}^{(i)} \tag{5.5}$$

where N_{frame} is the total number of frames.

(c) Nodal coordinates deviation

Although the surface-to-surface distance can be used to estimate the overall shape deviation from the simulation results, this measurement doesn't provides an estimation of the deviation of the dynamic movements at the sophisticated nodal level. For example, the FE surface may align well with the real surface of the human body, but the specific movements of the simulated nodes may greatly diverge with ground-truth movements. This may lead to the issue of identifying the true optimum material parameters, which is confirmed with the results in Subsection 5.4.1. In addressing this issue, the dense nodal coordinates were introduced for evaluation as follows:

Approach. Nodal trajectory deviation evaluation

1. Randomly select 100 nodes from the surface nodes as the representative landmarks.

2. Implement *virtual landmark tracking* (subsubsection (a)) at the

initial positions of these representative landmarks on the 4D scanning sequence. The estimated trajectories are considered as the ground-truth landmark trajectories.

3. Extract the trajectories of the representative landmarks from the FE simulation results. Estimate the averaged deviation from the ground-truth landmark trajectories:

$$d_{\text{coord}} = \frac{1}{N_{\text{frame}} N_{\text{node}}} \sum_{\text{i}=1}^{N_{\text{frame}}} \sum_{\text{j}=1}^{N_{\text{node}}} \|\hat{n}_j^{(i)} - \hat{m}_j^{(i)}\|_2 \tag{5.6}$$

where $\hat{n}_j^{(i)}$ is the j-th representative in the i-th frame and $\hat{m}_j^{(i)}$ is its corresponding ground-truth positions provided by the virtual landmark tracking.

(d) Nodal displacement deviation

Aside from the dense nodal trajectory, the dense nodal velocity is also important for describing the dynamic behavior/response of the soft-tissues of the breasts. Since the time intervals between the 4D scanning frames are identical, the nodal velocity is proportional to the frame-wise nodal displacement. Therefore, the deviation of the nodal displacement can be used to estimate the deviation of the FE simulation results on dense nodal velocity. The approach to evaluating the changes in nodal displacement is as follows:

Approach. Nodal displacement deviation evaluation

1. Randomly select 100 nodes from the surface nodes as the representative landmarks.

2. Implement *virtual landmark tracking* (subsubsection (a)) at the initial positions of these representative landmarks on the 4D scanning sequence. The estimated trajectories are considered as the ground-truth landmark trajectories.

3. Extract the trajectories of the representative landmarks from the FE simulation results. Estimate the averaged deviation from the ground-truth landmark trajectories:

$$d_{\text{disp}} = \frac{1}{N_{\text{frame}} N_{\text{node}}} \sum_{\text{i=1}}^{N_{\text{frame}}} \sum_{\text{j=1}}^{N_{\text{node}}} \|\Delta\hat{n}_j^{(i)} - \Delta\hat{m}_j^{(i)}\|_2 \tag{5.7}$$

where $\Delta\hat{n}_j^{(i)}$ is the frame-wise displacement of the j-th representative in the i-th frame and $\Delta\hat{m}_j^{(i)}$ is its corresponding ground-truth landmarks' frame-wise displacement.

5.2.3 Full domain optimization of material properties

(a) Principal parameters inflation scheme

As discussed in Subsection 5.2.1, the material properties of the soft tissues of the breasts are parameterized as a 5-dimensional vector: $p = (C_{10}, C_{01}, C_{11}, C_{20}, C_{02})$. Therefore, the optimization of the material parameters can be seen as a search problem in a 5-dimensional space. However, since the simulation of an FE model can typically take a few hours to complete depending on the complexity of the model and the simulated duration, it can be very time-consuming to obtain enough evaluation samples for an optimum parameter search. To address this issue, principal parameters inflation is proposed to transform the 5-dimensional space search problem to a 2-dimensional space search problem:

Approach. The principal parameters inflation scheme

1. Since the first 2 parameters (C_{10} and C_{01}) are the most influential parameters in Mooney-Rivlin material model, they are selected as the principal parameters.

2. Given value of C_{10} and C_{01}, other 3 parameters C_{11}, C_{20}, and C_{02} is inflated with a self-adjusting factor:

   (a) Generate the inflation factor β based on the ratio of Euclidean

lengths of (C_{10}, C_{01}) and $(C_{10}^{\text{origin}}, C_{01}^{\text{origin}})$:

$$\beta = \frac{\|(C_{10}, C_{01})\|_2}{\|(C_{10}^{\text{origin}}, C_{01}^{\text{origin}})\|_2} \tag{5.8}$$

where $(C_{10}^{\text{origin}}, C_{01}^{\text{origin}})$ is the original parameters presented in Subsection 5.2.1.

(b) Multiply C_{11}, C_{20}, and C_{02} with the inflation factor β to obtain the complete 5-dimension Mooney-Rivlin material parameter vector:

$$p = (C_{10}, C_{01}, \beta C_{11}^{\text{origin}}, \beta C_{20}^{\text{origin}}, \beta C_{02}^{\text{origin}}) \tag{5.9}$$

With principal parameters inflation, the search for the optimal parameters is conducted only on the principal parameters and the other parameters are generated accordingly. Although this method limits the searchable parameters to a subset of all applicable parameters, the approach can effectively reduce the resources needed for parameter optimization with physically reasonable near-optimum solutions.

(b) Loss function constructed with normalized metric fusion

For parameter optimization, the above mentioned 3 evaluation metrics (Subsection 5.2.2) need to be merged into a loss function. Since these metrics are estimated on different modalities, i.e. shape, coordinate, and displacement deviations, they typically result in different value ranges and are not appropriate to be summed up directly. In this case, normalization was introduced to the metric fusion algorithm for constructing the loss function:

Approach. Normalization based metric fusion

1. Given simulation results generated with a set of parameter vectors $P = \{p^a, p^a, ...\}$, the evaluation results form 3 sets:
   $D_{\text{shape}} = \{d_{\text{shape}}^a, d_{\text{shape}}^b, ...\}$ is a set of surface-to-surface distances.
   $D_{\text{coord}} = \{d_{\text{coord}}^a, d_{\text{coord}}^b, ...\}$ is a set of nodal coordinates deviations.
   $D_{\text{disp}} = \{d_{\text{disp}}^a, d_{\text{disp}}^b, ...\}$ is a set of nodal displacement deviations.

2. Obtain maximum and minimum value of D_{shape}, D_{coord} and D_{disp} and use them to define the metric normalization function:

   (a) Normalization function of surface-to-surface distance:

$$N_{\text{shape}}(d) = \frac{d - \min(D_{\text{coord}})}{\max(D_{\text{coord}}) - \min(D_{\text{coord}})} \tag{5.10}$$

   (b) Normalization function of nodal coordinates deviation:

$$N_{\text{coord}}(d) = \frac{d - \min(D_{\text{coord}})}{\max(D_{\text{coord}}) - \min(D_{\text{coord}})} \tag{5.11}$$

   (c) Normalization function of nodal displacement deviation:

$$N_{\text{disp}}(d) = \frac{d - \min(D_{\text{disp}})}{\max(D_{\text{disp}}) - \min(D_{\text{disp}})} \tag{5.12}$$

3. Define the metric fusion function (loss function):

$$L(d_{\text{shape}}, d_{\text{coord}}, d_{\text{disp}}) = \sum_{\text{metric}\in\{\text{shape,coord,disp}\}} \alpha_{\text{metric}} N_{\text{metric}}(d_{\text{metric}}) \tag{5.13}$$

   where $\alpha_{\text{shape}}, \alpha_{\text{coord}}, \alpha_{\text{disp}}$ are adjustable weights of different metrics. It's required that $\alpha_{\text{shape}} + \alpha_{\text{coord}} + \alpha_{\text{disp}} = 1$.

The complete workflow of the loss function estimation is illustrated in Figure 5.4.

(c) Interpolation based parameter optimization scheme

The loss function estimation workflow is firstly carried out on initial parameter samples. Based on these data samples, the continues metric plane on 2-dimension principal parameter space can be interpolated based on Thin Plate Spline (TPS) (Duchon, 1977). With the interpolated continues loss function plane, the material parameters can be optimized on the 2-dimension principal parameters space:

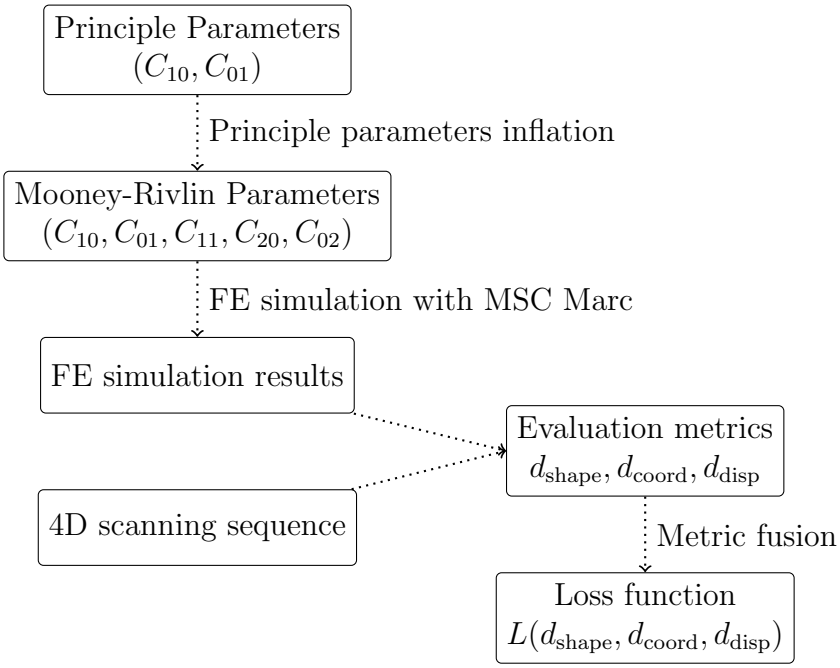

Figure 5.4: Flowchart of loss function estimation

Approach. Interpolation based parameter optimization scheme

1. Estimate loss function on the initial parameter samples.

2. Implement parameter optimization.

   (a) Interpolate the continues loss function plane on the principal parameters space.

   (b) Search the minimum loss value over the principal parameters space based on Nelder-Mead method (Gao & Han, 2010). Implement principal parameter inflation scheme on the corresponding principal parameters $(C_{10}^{\text{optim}}, C_{01}^{\text{optim}})$ to obtained the iterated material parameters p^{optim}.

   (c) Search the material parameters in all simulated samples that provides the smallest loss value and denoted as $(C_{10}^{\text{sample}}, C_{01}^{\text{sample}})$. Implement principal parameter inflation

scheme on it to obtained the optimized material parameters from samples p^{sample}.

3. Optimization convergence check.

   (a) Calculate the Euclidean distance between p^{optim} and p^{sample}. Since the measurement of distance is in 5 dimensional Euclidean space with MPa as unit, the unit of the distance shall be MPa.

   (b) If the distance is lesser than 10^{-4} MPa, the optimization is converged and p^{sample} is outputted as the optimum material parameters.

   (c) Otherwise, the optimization isn't converged and the p^{optim} will be added as the parameter samples. Actual FE simulation and Loss function estimation will be carried out on this new parameters sample and repeat the optimization procedure from step 2(a).

5.3 Bra-breast interaction simulation

5.3.1 Construction of bra-breast contact model

While wearing a sport's bras, it typically undergoes significant deformation in order to conform with its wearer's body shape and size; therefore, it is inappropriate for us just simply scan an isolated one for constructing its three-dimensional (3D) geometric model. In our study , we have instead extracted surfaces from scanned images where female subjects wore them (as shown in Figure 5.5). We assume that these materials exhibit linear elasticity characterized by two key parameters - Young's Modulus E (MPa) and Poisson ratio ν (Sun et al., 2019a; Sun et al., 2021; Sun et al., 2019c).

Combining with the breast FE model constructed in Section 5.2, the complete bra-breast interaction model is contracted and its element types are summarized in Table 5.2.

Figure 5.5: FE sub-model of the sports bra.

Table 5.2: Element types of the sub-models of the FE bra-breast interaction model

FE Sub-model	Body Type	Mesh Type	Mesh Size
Breasts soft tissue	Deformable body	Tetrahedron	8 mm
Peripheral torso soft tissue	Deformable body	Tetrahedron	8 mm
Rigid torso	Rigid body	–	–
Sports bra	Shell body	Quadrilateral	8 mm

5.3.2 Simulation of breast deformation and bra-breast contact pressure

MSC Marc (Hexagon Ltd. Stockholm, Sweden) was used as FE simulation solver. To simulate the bra-breast interaction during fast walking activity, three load cases were applied to the FE model sequentially:

Loadcases. Bra-breast interaction during fast walking

1. Interference fit to simulate the pre-tension force.
   Pre-tension force exists when a sports bra is worn. This force can be simulated in FE analysis using an interference fit method. This load case is simulated as *static analysis*:

   (a) Shrink the bra sub-model with ratio of 0.97.

(b) Expand the area that requires assembly, i.e. the bra sub-model, through material elasticity.

(c) Once the assembly is complete, the bra sub-model reverts to its original size creating a connection and generating some pressure.

2. Apply gravity force on the gravity-free FE model.
   This load case is simulated as *static analysis*.

3. Apply displacement to the torso part.
   The displacement data was obtained from the landmark 1 from the *DynaBreastManual* dataset constructed in Chapter 3. Noted that the contact type of the breast soft tissue and the torso part are set as *glued interaction* so that the displacement of torso part will thereby initiate the displacement and deformation of the breast tissue. Total increment steps are set as 200 and each step contains a time interval of 5 ms, simulating totally 1s of fast walking as compatible with the 4D scanning sequence. This load case is simulated as *dynamic analysis*.

5.4 Result

5.4.1 Construction of subject-specific FE breast model

(a) Evaluation metrics on initial parameter samples

17 samples were taken from the principal parameter space, as illustrated in Figure 5.6. The loss function estimation workflow discussed in Subsection 5.2.3 was first applied to these initial parameter samples, summarized in Table 5.3. To enhance efficiency, a simulation management package named `FEcluster` was developed for *automatic material properties editing, simulation tasks scheduling and distribution across multiple computers.*The code for this package can be accessed at https://github.com/liu-qilong/FEcluster.

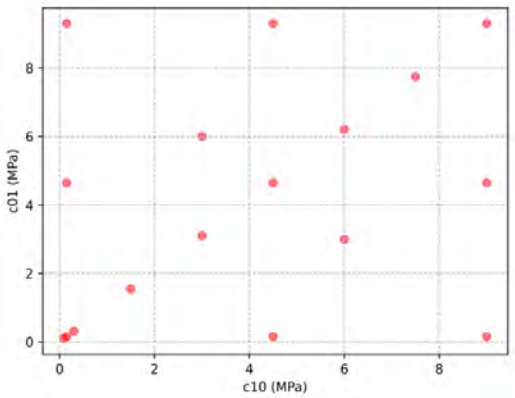

Figure 5.6: Initial parameter samples.

As shown in Figure 5.7, all evaluation metrics show a peak when dealing with smaller parameters (approximately when C_{01} and C_{10} are less than 0.3 kPa). For both surface-to-surface distance and nodal displacement deviation measures,the deviation stabilizes as parameters increase.This indicates that these metrics do not effectively differentiate between optimal parameters.However,the nodal trajectories metric displays a clear valley area which effectively narrows down the search area for optimal material parameters.

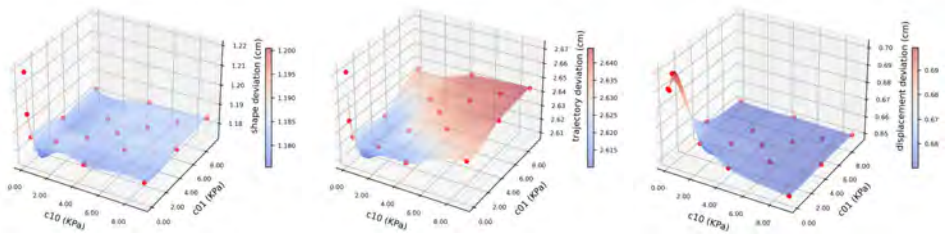

(a) (b) (c)

Figure 5.7: The interpolated continues metric plane on 2-dimension principal parameter: (a) surface-to-surface distance; (b) nodal coordinates deviation; and (c) nodal displacement deviation.

Table 5.3: Evaluation metrics on initial parameter samples

Mooney-Rivlin Parameters (kPa)					Evaluation Metric (cm)		
C_{10}	C_{01}	C_{11}	C_{20}	C_{02}	d_{shape}	d_{coord}	d_{disp}
0.09	0.09	0.68	1.42	1.14	1.22	2.67	0.69
0.15	0.15	1.12	2.36	1.90	1.20	2.64	0.69
0.30	0.31	2.25	4.72	3.80	1.19	2.63	0.70
3.00	3.10	22.50	47.20	38.00	1.18	2.63	0.66
4.50	4.65	33.75	70.80	57.00	1.18	2.64	0.65
6.00	6.20	45.00	94.40	76.00	1.18	2.64	0.65
7.50	7.75	56.25	118.00	95.00	1.18	2.64	0.65
9.00	9.30	67.50	141.60	114.00	1.18	2.64	0.65
1.50	1.55	11.25	23.60	19.00	1.18	2.62	0.66
0.15	4.65	24.26	50.90	40.98	1.18	2.62	0.66
0.15	9.30	48.51	101.77	81.93	1.18	2.64	0.65
3.00	6.00	34.99	73.40	59.09	1.18	2.63	0.65
4.50	0.15	23.48	49.27	39.66	1.18	2.62	0.66
4.50	9.30	53.89	113.04	91.01	1.18	2.64	0.65
6.00	3.00	34.99	73.40	59.09	1.18	2.63	0.65
9.00	0.15	46.95	98.49	79.29	1.18	2.63	0.65
9.00	4.65	52.84	110.84	89.23	1.18	2.64	0.65

(b) Optimized Mooney-Rivlin coefficient

Considering various metrics' abilities to distinguish optimal parameters, we set $\alpha_{\text{shape}}, \alpha_{\text{coord}}, \alpha_{\text{disp}}$ at 0.2, 0.8, and 0.2 respectively for metric fusion purposes. The data samples from our loss function along with its continuous interpolated plane are depicted in Figure 5.8.

As per our discussion on optimization schemes in Subsection 5.2.3, during our first round of optimization we determined that $(1.029, 1.022, 7.565, 15.870, 12.777)$ were indeed optimized Mooney-Rivlin material properties (Figure 5.9a). However since this particular parameter's proximity to its minimum within all sampled parameters stood at 1.06×10^{-2} MPa, the optimization wasn't converged and the actual loss function evaluation was carried out on these new parameter sample.

At the second round of optimization, the optimized Mooney-Rivlin

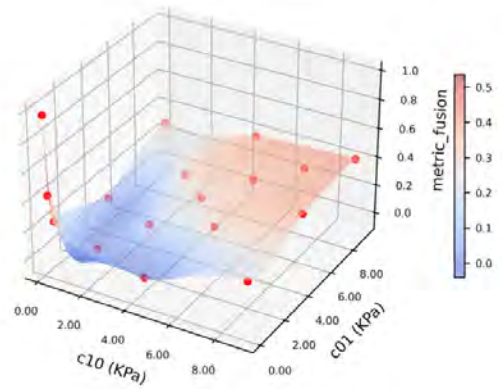

Figure 5.8: Metric fusion on the initial parameter samples.

material properties was $(1.031, 1.019, 7.563, 15.866, 12.774)$, as shown in Figure 5.9b. Since the distance of this parameter to the minimum in the parameter samples was 6.48×10^{-6} (MPa), the optimization was converged. The minimum in the parameter samples, $(1.029, 1.022, 7.565, 15.870, 12.777)$, was outputted as the optimized Mooney-Rivlin material parameters of the subject-specific FE model.

(c) Verification of breast material parameters

As shown in Table 5.4, the optimized Mooney-Rivlin material parameters achieved the lowest deviation values for surface-to-surface deviation d_{shape} and nodal coordinates deviation d_{coord}. For nodal displacement deviation d_{disp}, though the optimized parameters doesn't achieved the lowest value but remains in compatible range with the optimum parameters. For metric fusion value, the optimized material parameters achieve a significantly lower value comparing with other parameter samples, indicating a generally more realistic parameterization of the breast dynamic characteristics of the female subject.

For qualitatively evaluation, the breast deformation simulation results with the optimized material parameters were plotted with the ground-truth 4D scanning sequence. As shown in Figure 5.10, the movement of the breast aligned well with the swinging movement of the female subject during the fast

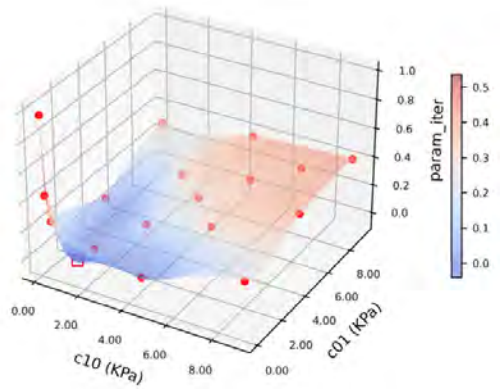

(a) Iteration 1

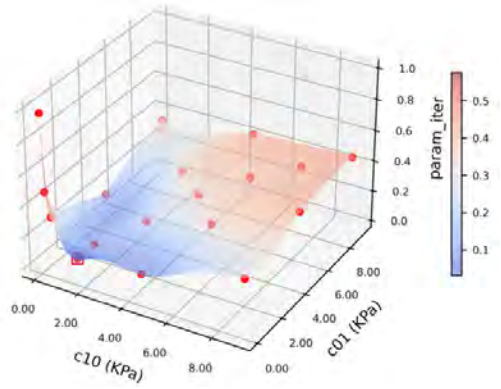

(b) Iteration 2

Figure 5.9: Parameter iterations. Note that the red dots represent the evaluated parameter samples while the red rectangle represents the estimated optimized parameter.

walking, verifying the applicability of the constructed FE model for breast biomechanics simulations.

5.4.2 Control performance analysis of sports bra based on FE contact model

With the optimized breast Mooney-Rivlin parameters, the bra-breast contact model can then be constructed. By modifying material properties of the sports bra, the biomechanical performance of the sports bras with different

Table 5.4: Evaluation metrics on initial parameter samples and the optimized parameter. The optimized parameters are marked with *.

Mooney-Rivlin Parameters (kPa)					Evaluation Metric (cm)			Metric Fusion
C_{10}	C_{01}	C_{11}	C_{20}	C_{02}	d_{shape}	d_{coord}	d_{disp}	L
0.09	0.09	0.68	1.42	1.14	1.22	2.67	0.69	0.98
0.15	0.15	1.12	2.36	1.90	1.20	2.64	0.69	0.49
0.30	0.31	2.25	4.72	3.80	1.19	2.63	0.70	0.32
3.00	3.10	22.50	47.20	38.00	1.18	2.63	0.66	0.21
4.50	4.65	33.75	70.80	57.00	1.18	2.64	0.65	0.33
6.00	6.20	45.00	94.40	76.00	1.18	2.64	0.65	0.40
7.50	7.75	56.25	118.00	95.00	1.18	2.64	0.65	0.43
9.00	9.30	67.50	141.60	114.00	1.18	2.64	0.65	0.44
1.50	1.55	11.25	23.60	19.00	1.18	2.62	0.66	0.10
0.15	4.65	24.26	50.90	40.98	1.18	2.62	0.66	0.15
0.15	9.30	48.51	101.77	81.93	1.18	2.64	0.65	0.34
3.00	6.00	34.99	73.40	59.09	1.18	2.63	0.65	0.33
4.50	0.15	23.48	49.27	39.66	1.18	2.62	0.66	0.15
4.50	9.30	53.89	113.04	91.01	1.18	2.64	0.65	0.42
6.00	3.00	34.99	73.40	59.09	1.18	2.63	0.65	0.33
9.00	0.15	46.95	98.49	79.29	1.18	2.63	0.65	0.33
9.00	4.65	52.84	110.84	89.23	1.18	2.64	0.65	0.42
1.03*	1.02*	7.56*	15.87*	12.78*	1.18	2.61	0.66	0.03

material properties can therefore be realistic simulated.

Sun et al. (2019c) conducted material tests on different bra components' fabrics. The Young's modulus values are ranging from 0.1 to 1 MPa with almost identical Poisson ratio of 0.3. In this research, to simulate the performance of bra materials with different stiffness, 3 settings of the sports bra material properties were selected for simulation, with increasing Young's modulus from 0.10 MPa to 1.00 MPa and an identical poisson ratio of 0.30. The breasts nodal displacement related to the torso and the contact pressure with the sports bra are selected as the evaluation metrics of the sports bras' performance.

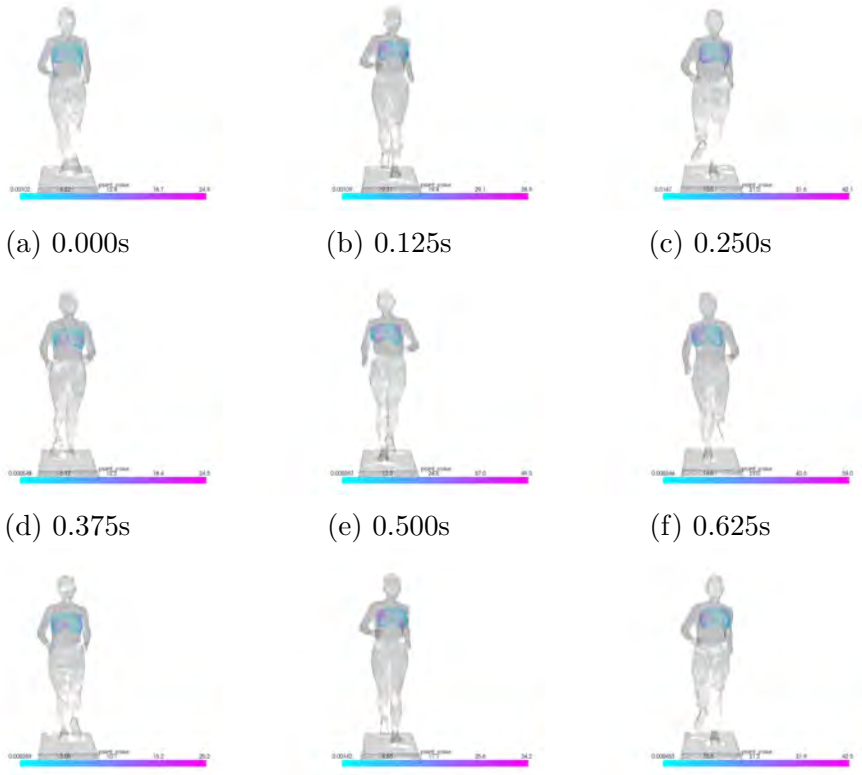

(a) 0.000s (b) 0.125s (c) 0.250s

(d) 0.375s (e) 0.500s (f) 0.625s

(g) 0.750s (h) 0.875s (i) 1.000s

Figure 5.10: Breast deformation simulation results plotted with the ground-truth 4D scanning sequence. Note that the simulated nodes are colored with surface-to-surface distance and the unit is mm.

(a) Overall breasts displacement and pressure pattern

As shown in Table 5.5 and Figure 5.11, with the increment of the Young's modulus, the sports bras materials become more rigid and the relative displacements of the breasts become lower, while the contact pressures become larger. However, when the Young's modulus are larger than 0.50 MPa, the reduce of the breasts' relative displacements become non-significant while the contact pressure still increases prominently: the averaged relative displacement of 1.00 MPa Young's modulus bra decreases 6.08% comparing with 0.50 MPa Young's modulus bra, while the contact pressure increases 78.57%. According to previous studies, the acceptable range for comfortable

clothing pressure on the human body is typically between 1.96 and 3.92 kPa, taking into account individual variations and different body areas (Song & Feng, 2006). The contact pressure of the 1.00 MPa Young's modulus bra is significantly larger than this range, indicating that the bra with such a large Young's modulus may cause discomfort to the wearer.

Table 5.5: Statistical analysis of relative displacement and contact pressure of different sports bra materials properties (Young's modulus E and Poisson ratio ν).

Material Properties		Relative Displacement (cm)				Peak Contact Pressure (kPa)			
E (MPa)	ν	min	max	mean	std	min	max	mean	std
0.10	0.30	13.25	51.37	19.12	7.08	0.00	7.42	0.07	0.31
0.50	0.30	13.24	38.12	18.09	5.48	0.00	18.89	0.28	0.65
1.00	0.30	13.24	36.42	17.98	5.20	0.00	27.82	0.50	0.93

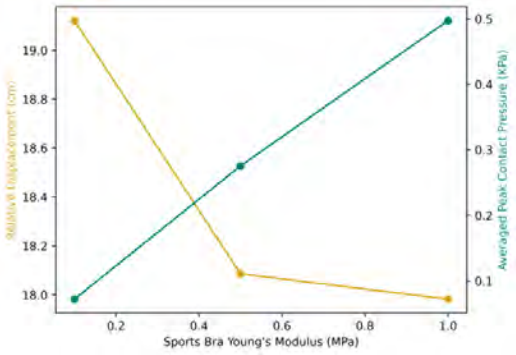

Figure 5.11: Curves of relative displacement and contact pressure across different Young's modulus of sports bra.

The distribution of contact pressure is illustrated in Figure 5.12. As Young's modulus increases from 0.10 MPA to 1.00 MPa, there is a rapid increase in contact pressure on both the side and front areas of the breasts, as well as on the shoulder straps; however, changes near the sternum area remain negligible. This suggests an increasingly uneven distribution of pressure which could potentially lead to discomfort or even negative health effects.

The result indicates that although increasing the Young's modulus of the sports bra can enhance the sports bra's performance on controlling breasts

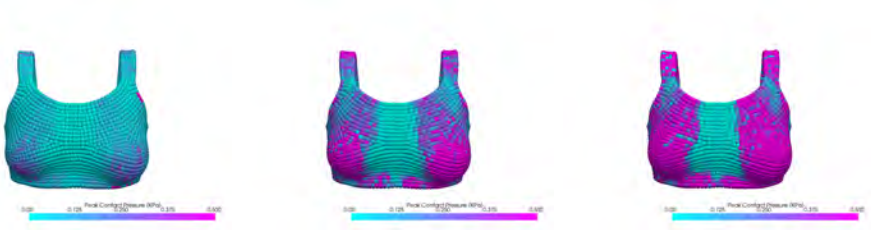

(a) 0.10 MPa (b) 0.50 MPa (c) 1.00 MPa

Figure 5.12: Contact pressure distribution of different sports bra materials with different settings of Young's modulus.

movement, a too large Young's modulus may also expose risk on posing too much contact pressure onto the wearer. This relative displacement and contact pressure curves obtained in this research may provide data for the designer to select a proper sports bra material with optimum stiffness with balancing performance on the breasts movement control and the contact pressure control.

(b) Breasts regional displacement and pressure pattern

To facilitate more detailed understanding of the breasts displacement and contact pressure in different breasts area when wearing sports bras with different stiffness, simulation results of the *shoulder straps*, *bra band*, and the *bottom breasts* areas were extracted for further analysis, as shown in Table 5.6 and Figure 5.13. Results shown that the bottom breasts area undergoes the largest relative displacement as well as the largest contact pressure, with all settings of bra materials. As the Yound's modulus of the bra material increases, the contact pressure of all breasts areas increases significantly while the relative displacements of the breasts only has slight decreases for the bottom breasts area and has almost imperceivable changes for the shoulder straps and the bra band areas.

This indicates that sports bra design should place more attention on the bottom breasts area as it's more susceptible to displacement and pressure. The material stiffness of the sports bra also plays a crucial role in determining the comfort and support level for wearers. While stiffer materials may

Table 5.6: Regional statistical analysis of relative displacement and contact pressure of different sports bra materials properties (Young's modulus E and Poisson ratio ν).

Material Properties		Region	Relative Displacement (cm)				Peak Contact Pressure (kPa)			
E (MPa)	ν		min	max	mean	std	min	max	mean	std
0.10	0.30	strap	13.25	13.34	13.27	0.02	0.00	0.21	0.07	0.06
		band	13.25	13.75	13.32	0.09	0.07	0.42	0.05	0.05
		bottom	13.26	42.37	33.59	6.53	34.21	2.59	0.21	0.29
0.50	0.30	strap	13.24	13.68	13.38	0.14	0.00	1.03	0.33	0.30
		band	13.25	14.03	13.41	0.16	54.01	0.92	0.24	0.14
		bottom	13.26	38.08	31.47	5.44	36.67	2.22	0.66	0.34
1.00	0.30	strap	13.22	14.08	13.53	0.28	0.00	1.87	0.63	0.56
		band	13.26	14.47	13.54	0.26	97.67	1.57	0.44	0.22
		bottom	13.26	35.88	30.53	4.54	41.96	2.16	1.14	0.46

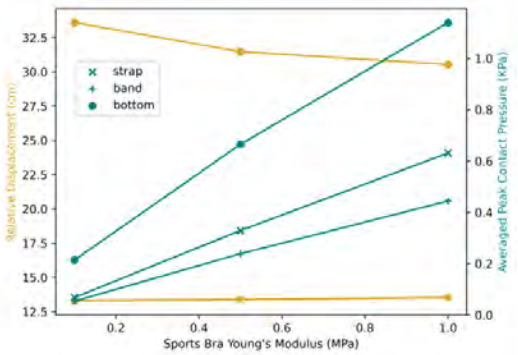

Figure 5.13: Curves of relative displacement and contact pressure across different Young's modulus of different sports bra areas.

provide better support by reducing relative displacements, they can also lead to increased contact pressure which might cause discomfort or even pain during physical activities. Therefore, an optimal balance between material stiffness and comfort needs to be achieved in sports bra design. Moreover, it's worth noting that despite the slight decrease in relative displacements with increasing Young's modulus, there are almost no changes observed for shoulder straps and bra band areas. This suggests that these areas are less affected by the material properties of the bras compared to the bottom

breasts area. In conclusion, our findings suggest that more focus should be placed on designing sports bras that offer adequate support at the bottom breasts area without causing excessive contact pressure. Further studies could explore different combinations of materials or innovative designs to achieve this goal while ensuring overall comfort for wearers during physical activities.

5.5 Conclusion

In this chapter, a subject-specific FE biomechanics model of the breast was constructed. For the first time, 4D scanning sequences were introduced as supervision signals for determining subject-specific hyper-elasticity parameters for breasts. Three evaluation metrics were created for optimization: surface-to-surface distance, nodal coordinates deviation and nodal displacement deviation based on the UdMC algorithm proposed in Chapter 4. With these metrics achieving distances and deviations within acceptable ranges during testing, we verified that our optimized hyper-elastic properties are applicable for realistic breast biomechanics simulation.

Using these verified material properties for breasts allowed us to construct a bra-breast interaction model which simulates ergonomic performance of sports bras made from different materials - providing critical information previously only obtainable through time-consuming wear trials. This chapter investigated how changes in a sports bra's modulus affected relative breast displacement and bra-breast contact pressure. Results showed that while increasing sportswear material's Young's modulus can improve movement control of breasts; too large a Young's modulus may risk applying excessive contact pressure onto wearers and the pressure distribution may become increasingly uneven.

To the best of our knowledge, this is the first approach that using high-temporal and spatial dynamic scanning of breasts to determine subject-specific parameters for biomechanical simulation models – offering significant potential towards comprehensive understanding of breast biomechanics research as well as supporting wearable product design.

Chapter 6
Conclusions and Suggestions for Future Research

6.1 Conclusions

The primary goal of the research was to advance the FE model on the basis of the novel 4D body scanning technology. With reference to the regional deformation behaviour of the soft breast tissues during continuous body movements, bra designers can better understand the effects of bra features and materials on control of breast displacements for optimal support and protection.

The project objectives, which are discussed in detail in Section 1.2, have been realized and the achievements of the research are summarized as follows:

1. In Chapter 3, to effectively capture the dynamic breast deformation in vivo with high temporal and spatial resolutions, the 4D body scanning technology was applied. The surface changes and stretching of the skin of the breasts, and changes of the geometry of the breast shape during dynamic motion were analyzed. Based on the data collected data and the `mesh4d` toolkit, a breast anthropometric dataset named *DynaBreastManual* was constructed. In-depth analysis of the in vivo breast deformation patterns were carried out based on this dataset, confirming existing studies on breast deformation patterns as well as extending them to a detailer and clearer presentation of the dynamic

characteristics of the breast with 4D scanning data. Several conclusions are drawn from the obtained data:

(a) The study found that the primary movements of breasts during fast walking are vertical and lateral swinging, with less variation in forward and backward movements.

(b) The landmarks on the left and right breast areas show opposite movement trends due to the swinging motion during fast walking.

(c) Spatial trajectories of different landmarks form a butterfly-like pattern, confirming previous research on complex breast movement patterns.

(d) Accumulated trajectory lengths range from 50 cm to 80 cm within nearly one second of recording, indicating significant deformation.

(e) Deformation intensity increases smoothly from chest to nipple areas; soft tissues are more deformable than rigid torso areas.

(f) Directional analysis shows large medial-lateral deformations in entire breast area and chest area while only soft tissues experience obvious vertical deformation. Forward-backward deformations occur mainly on side-parts of torso.

2. In Chapter 4, to efficiently track specific key points in arbitrary positions to characterize the surface motion and deformation of the soft tissues of the breasts to model the biomechanics of the breasts, a semi-automatic method is proposed namely the Ultra-dense Motion Capture (UdMC) algorithm. With a 4D scanning sequence marked with sparse anatomical landmarks, UdMC can reveal the dense whole-surface deformation profile of the scanned object robustly. Comprehensive evaluation of the proposed methods indicates that the UdMC significantly excels the comparison baselines in terms of accuracy, consistency, and efficiency:

   (a) The UdMC algorithm shows the lowest alignment error across all sub-datasets, demonstrating its reliability and consistency in

accurate alignments.

(b) Compared to other models, the UdMC consistently performs better, especially as frame rates increase and sequences lengthen. This indicates its superior scalability - a crucial factor for practical applications.

(c) Unlike other algorithms whose errors rapidly accumulate over successive frames, the UdMC maintains stable performance throughout the entire process. This suggests that it is more reliable and robust for tracking breast motion.

(d) In terms of capturing overall pattern of breast movement, only proposed approach effectively captures complex dynamics accurately.

(e) Two downstream tasks are introduced to demonstrate the practical application of the UdMC algorithm: (i) tracking virtual landmarks in an arbitrary position without attaching physical markers to the region, and (ii) estimating deformation intensity for fine-granularity during dynamic activities.

3. In Chapter 5, a subject-specific FE model to simulate the contact mechanics between a sports bra and the breasts on the basis of the behavior and motion of the breasts is established. For the first time, 4D scanning sequences were introduced as supervision signals for determining subject-specific hyper-elasticity parameters for breasts. Three evaluation metrics were created for optimization: surface-to-surface distance, nodal coordinates deviation and nodal displacement deviation based on the UdMC algorithm. With the optimized material properties for breasts, a bra-breast interaction model was constructed for simulating the ergonomic performance of sports bras made from different materials, leading to critical information previously only obtainable through time-consuming wear trials. Several conclusions are draw from the obtained data:

(a) Only with 2 iterations, the optimized subject-specific

Mooney-Rivlin material properties are converged at $(C_{10}, C_{01}, C_{11}, C_{20}, C_{02}) = (1.029, 1.022, 7.565, 15.870, 12.777)$ (KPa).

(b) This study provides data that can help designers select optimal stiffness level for sports bra materials balancing performance on controlling breast movement and managing contact pressure effectively.

4. To evaluate the regional deformation and contact pressure of the breasts in response to different bra materials, through FE analyzes and experimental measurements, in Subsection 5.4.2, the breast displacement control performance and the contact pressure levels with different bra material settings are simulated and analyzed:

(a) Three settings of sports bra material properties were selected for simulation with increasing Young's modulus from 0.10 MPa to 1.00 MPa and shared poisson ratio of 0.30. As Young's modulus increased, sports bras became more rigid leading to lower relative displacements but higher contact pressures on breasts.

(b) However beyond a certain point (Young's modulus larger than 0.50MPa), reduction in relative displacement becomes insignificant while contact pressure continues to increase significantly indicating potential discomfort or harm to wearer due to excessive pressure despite better control over breast movement.

(c) Regional analysis showed that as Young's modulus increases from 0.10 MPA to 1.00 MPa, there is a rapid increase in contact pressure on both the side and front areas of the breasts, as well as on the shoulder straps; however, changes near the sternum area remain negligible. This suggests an increasingly uneven distribution of pressure which could potentially lead to discomfort or even negative health effects.

(d) Among the shoulder straps, the bottom breasts, and the bra band areas, the study found that the bottom breasts area experiences the most displacement and pressure when wearing sports bras of varying stiffness, indicating a need for designs that provide adequate support in this area without causing excessive discomfort.

5. To compare and validate the breast deformation results of a computational FE model with the experimental results, in Subsection 5.4.1, the deviation between the simulated breasts behaviors and the ground-truth data extracted from the 4D scanning sequence are systematically evaluated:

   (a) In all simulated parameter samples, the optimized parameters achieved lowest deviation values for surface-to-surface deviation and nodal coordinates deviation while maintaining a compatible range with optimum parameters for nodal displacement deviation.

   (b) Qualitative evaluation showed good alignment between simulated breast movement and actual movement during fast walking which verifies applicability of constructed FE model for breast biomechanics simulations.

6.2 Contributions

In Chapter 3, we investigated the potential of dynamic breast deformation analysis based on the high-temporal and spatial resolution 4D scanning sequence. Compared with previous works on breast dynamic deformation patterns based on MoCap (Sohn & Bye, 2014; Zhou et al., 2011, 2012), the recording and analyzing of the breast dynamic behavior was advanced from sparse landmarks level to the continues surface levels, providing much higher granularity data for breast anthropometric measurements and analysis.

In Chapter 4, we investigated the registration of dynamic surface in the 4D scanning sequence to provide the dense whole-surface deformation profile.

Establishing dense-correspondence between deformable surfaces remains a challenging problem. While geometric shape information can provide crucial information, this alone cannot completely solve this problem. For example, if a cylinder rotating along its axis is scanned, the outputs will be identical three-dimensional (3D) meshes over time. In this case, it is not possible to identify the rotation movement solely based on the scanned geometric shapes. As reported in Bogo et al. (2017), a significant accuracy gap was observed between geometric-only versus texture incorporated registration schemes, thus emphasizing the importance of incorporating other modalities when establishing dense correspondence between surfaces. The approach in this study involves anatomical landmarks with known inter-frame correspondence which provides an initially near-optimal alignment, and leads to a large margin of improvement in efficiency and accuracy compared with the calculation costly iterations in geometric-only registration methods.

Designing an approach that effectively merges information from different modalities is challenging. The ECPD algorithm (Golyanik et al., 2016) integrates sparse prior correspondence information within the CPD framework by multiplying the alignment term of the prior correspondence with the surface alignment term as an objective function, thereby resulting in surface alignment optimization by following guidance from the prior correspondence. However, as demonstrated in Section 4.3, this method does not yield superior quantitative and qualitative results compared to state-of-the-art geometric-only methods such as the CPD (Myronenko & Song, 2010) and BCPD (Hirose, 2021) algorithms. This is likely due to the sparse nature of prior correspondence - where the alignment term of the prior correspondence has less influence than the surface alignment term. In contrast, the proposed approach uses TPS interpolation for establishing the initial prior dense correspondence which is then rectified by using geometric information from a 4D scanning sequence. This technique is an improvement over prior correspondence information. The evaluation results indicate that this simple technique significantly improves both accuracy and calculation efficiency.

With 4D scanning technology and the proposed UdMC algorithm, we

provide a rigour tool to record, digitize, and analyze the dynamic surface of a deformable object. Comparing with traditional methods like MoCap and 3D scanning, our proposed approach provides the most holistic information, as summarized in Table 6.1. In lights of the advantages it provides, the proposed approach may have great potentials to advance anthropometry studies at the sparse-landmark level to dense-surface level, thus enabling more comprehensive analyses and understanding of the dynamic deformation patterns and properties of breasts.

Table 6.1: Comparison between different techniques/approaches for record, digitize, and analyze the an object's motion and geometry.

	Landmark Tracking		Surface Scanning	
Device	Sparse	Dense	Static	Dynamic
MoCap	✓	×	×	×
3D scanner	×	×	✓	×
4D scanner	×	×	✓	✓
4D scanner with UdMC	✓	✓	✓	✓

In Chapter 5, a complete workflow was established for fine-tuning the subject-specific hyper-elasticity parameters based on 4D scanning sequences. A bra-breast interaction model was then constructed to simulate sports bras' Young's modulus effects on relative breast displacement and bra-breast contact pressure. Compared to prior work (del Palomar et al., 2008; Sun et al., 2019a; Sun et al., 2019b; Sun et al., 2021; Sun et al., 2019c) that only utilized static 3D images scanned with a 3D scanner and sparse landmark locations recorded with MoCap systems, this approach provides dynamic deformation information about breasts at much higher granularity levels leading to more realistic and reliable determinations of breast material parameters - crucial for realistic biomechanical simulations of breasts for biomechanics research as well as providing design insights for wearable product designers.

6.3 Suggestions for future research

Due to the pioneering nature of this approach, several limitations need to be addressed in future work.

For the constructed dynamic breasts anthropometric dataset *DynaBreastManual* in Chapter 3: (i) the method depends on manually labelling the anatomical landmarks, so that it is only semi-automatic and potentially introduces errors due to human intervention. Even though the UdMC is not fully automatic, manually labeling a few landmarks to establish a dense motion profile of the entire surface of the breast may serve as an effective alternative compared with entirely manual approaches. Future research could investigate the use of motion capture (MoCap) devices to automate the labelling process, which would enhance both efficiency and accuracy; (ii) occasionally, it was observed that the scanned mesh sequence contains holes and breaches in the lower area of the breast due to insufficient optical cameras pointing towards these perspectives. Consequently, some of the landmarks were discarded as discussed in Subsection 3.2.2. To rectify this issue, it is crucial to create a more comprehensive multi-view camera setting by increasing camera density and balancing their placement; (iii) although we scanned the entire surface area of each breast, our analysis focused solely on displacement at sparse landmark points. To address this limitation, the UdMC algorithm was proposed to reveal the dense whole-surface deformation profile, as will be discussed in Chapter 4.

For the proposed UdMC algorithm in Chapter 4: (i) the registration implementation in this study uses a simple sequential alignment scheme that might suffer from cumulative inter-frame errors. More advanced long and short range alignment techniques (Bogo et al., 2017) could further improve the accuracy; and (ii) the *DynaBreastManual* dataset used for evaluation consists of 18 anthropometric landmarks across 121 frames of 3D reconstructed scenes that total 2178 ground-truth landmark coordinates. However, it should be noted that all of the data were collected from one subject fast walking at a speed of 6 km/h. This dataset was created specifically for validating the proposed method with carefully constructed

ground truth but currently remains limited to the subject- and case-specific levels. In future studies, the plan is to expand this dataset by including more subjects and covering a broader range of dynamic activities to facilitate data diversity.

For the 4D data supervised breast hyper-elasticity parameter determination workflow proposed in Chapter 5: (i) as shown in Subsection 5.4.1, optimized material parameters achieved surface-to-surface distances of 1.18 cm, nodal coordinates deviation of 2.61 cm, and nodal displacement deviations of 0.66 cm, indicating there is still significant room for accuracy improvement. Nevertheless, since the accuracy evaluations are carried out with high-granularity dynamic information from the 4D scanning sequence, the evaluation of the simulation accuracy is actually much stricter than previous works (del Palomar et al., 2008; Sun et al., 2019a; Sun et al., 2019b; Sun et al., 2021; Sun et al., 2019c). It is understandable that the evaluation metrics seem worse than those from previous studies; and (ii) For treadmill fast walking simulations, only the torso displacement was inputted as boundary conditions while the torso rotation was neglected. As rotation constitutes a large portion of torso movement during treadmill fast walking, this omission limits the simulation system's accuracy. Future research may investigate on introducing rotational movement for more realistic biomechanical breast simulations which in turn would guarantee more accurate determination of subject-specific hyper-elastic parameters for breasts.

Bibliography

Al-Anezi, T., Khambay, B., Peng, M., O'Leary, E., Ju, X., & Ayoub, A. (2013). A new method for automatic tracking of facial landmarks in 3d motion captured images (4d). *International Journal of Oral and Maxillofacial Surgery*, *42*(1), 9–18. https://doi.org/10.1016/j.ijom.2012.10.035

Arch, E. S., Colón, S., & Richards, J. G. (2018). A comprehensive method to measure 3-dimensional bra motion during physical activity. *Journal of Applied Biomechanics*, *34*(5), 392–395. https://doi.org/10.1123/jab.2017-0111

Bartol, K., Bojanic, D., Petkovic, T., & Pribanic, T. (2021). A review of body measurement using 3d scanning. *IEEE Access*, *9*, 67281–67301. https://doi.org/10.1109/access.2021.3076595

Behrenbruch, C. P., Marias, K., Armitage, P. A., Yam, M., Moore, N., English, R. E., Clarke, J., & Brady, M. (2003). Fusion of contrast-enhanced breast MR and mammographic imaging data. *Medical Image Analysis*, *7*(3), 311–340. https://doi.org/10.1016/s1361-8415(03)00015-x

Bernardini, F., Mittleman, J., Rushmeier, H., Silva, C., & Taubin, G. (1999). The ball-pivoting algorithm for surface reconstruction. *IEEE Transactions on Visualization and Computer Graphics*, *5*(4), 349–359. https://doi.org/10.1109/2945.817351

Besl, P., & McKay, N. D. (1992). A method for registration of 3-d shapes. *IEEE Transactions on Pattern Analysis and Machine Intelligence*, *14*(2), 239–256. https://doi.org/10.1109/34.121791

Bishop, C. M. (2016). *Pattern recognition and machine learning*. Springer New York.

Bogo, F., Romero, J., Loper, M., & Black, M. J. (2014). Faust: Dataset and evaluation for 3d mesh registration. *Proceedings of the IEEE Conference on Computer Vision and Pattern Recognition (CVPR)*.

Bogo, F., Romero, J., Pons-Moll, G., & Black, M. J. (2017). Dynamic FAUST: Registering human bodies in motion. *2017 IEEE Conference on Computer Vision and Pattern Recognition (CVPR)*. https://doi.org/10.1109/cvpr.2017.591

Bowles, K. A., & Steele, J. (2013). Effects of strap cushions and strap orientation on comfort and sports bra performance. *Medicine & Science in Sports & Exercise*, *45*(6), 1113–1119. https://doi.org/10.1249/mss.0b013e3182808a21

Bowles, K. A., Steele, J., & Munro, B. (2012). Features of sports bras that deter their use by australian women. *Journal of Science and Medicine in Sport*, *15*(3), 195–200. https://doi.org/10.1016/j.jsams.2011.11.248

Chen, L. H., Ng, S. P., Yu, W., Zhou, J., & Wan, K. (2013). A study of breast motion using non-linear dynamic fe analysis. *Ergonomics*, *56*(5), 868–878. https://doi.org/10.1080/00140139.2013.777798

Chen, Y., & Medioni, G. (1992). Object modelling by registration of multiple range images. *Image and Vision Computing*, *10*(3), 145–155. https://doi.org/10.1016/0262-8856(92)90066-c

Chi, L., & Kennon, R. (2006). Body scanning of dynamic posture. *International Journal of Clothing Science and Technology*, *18*(3), 166–178. https://doi.org/10.1108/09556220610657934

Choi, J., & Hong, K. (2015). 3d skin length deformation of lower body during knee joint flexion for the practical application of functional sportswear. *Applied Ergonomics*, *48*, 186–201. https://doi.org/10.1016/j.apergo.2014.11.016

Choi, S., & Ashdown, S. (2011). 3d body scan analysis of dimensional change in lower body measurements for active body positions. *Textile Research Journal*, *81*(1), 81–93. https://doi.org/10.1177/0040517510377822

Chowdhury, H., Alam, F., Mainwaring, D., Beneyto-Ferre, J., & Tate, M. (2012). Rapid prototyping of high performance sportswear. *Procedia Engineering*, *34*, 38–43. https://doi.org/10.1016/j.proeng.2012.04.008

Coltman, C., Steele, J., & Mcghee, D. (2018). Which bra components contribute to incorrect bra fit in women across a range of breast sizes? *Clothing and Textiles Research Journal*, *36*(2), 78–90. https://doi.org/10.1177/0887302x17743814

Costa, I. F. (2012). A novel deformation method for fast simulation of biological tissue formed by fibers and fluid. *Medical Image Analysis*, *16*(5), 1038–1046. https://doi.org/10.1016/j.media.2012.04.002

Dan, R., Fan, X. R., Xu, L. B., & Zhang, M. (2011). Numerical simulation of the relationship between pressure and material properties of the top part of socks. *Journal of the Textile Institute*, *104*(8), 844–851. https://doi.org/10.1080/00405000.2012.758516

del Palomar, A. P., Calvo, B., Herrero, J., López, J., & Doblaré, M. (2008). A finite element model to accurately predict real deformations of the breast. *Medical Engineering & Physics*, *30*(9), 1089–1097. https://doi.org/10.1016/j.medengphy.2008.01.005

den Herrewegen, I. V., Cuppens, K., Broeckx, M., Barisch-Fritz, B., Sloten, J. V., Leardini, A., & Peeraer, L. (2014). Dynamic 3d scanning as a markerless method to calculate multi-segment foot kinematics during stance phase: Methodology and first application. *Journal of Biomechanics*, *47*(11), 2531–2539. https://doi.org/10.1016/j.jbiomech.2014.06.010

Diez, Y., Oliver, A., Llado, X., & Marti, R. (2010, September). Comparison of registration methods using mamographic images. *2010 ieee international conference on image processing* (pp. 4421–4424). IEEE. https://doi.org/10.1109/icip.2010.5653325

Domingo, J., Ibáñez, M., Simó, A., Dura, E., Ayala, G., & Alemany, S. (2014). Modeling of female human body shapes for apparel design based on cross mean sets. *Expert Systems with Applications*, *41*(14), 6224–6234. https://doi.org/10.1016/j.eswa.2014.04.014

Doyley, M. M. (2012). Model-based elastography: A survey of approaches to the inverse elasticity problem. *Physics in Medicine and Biology*, *57*(3), R35–R73. https://doi.org/10.1088/0031-9155/57/3/r35

Duchon, J. (1977). Splines minimizing rotation-invariant semi-norms in sobolev spaces. *Constructive theory of functions of several variables* (pp. 85–100). Springer Berlin Heidelberg. https://doi.org/10.1007/bfb0086566

Edelsbrunner, H., Kirkpatrick, D., & Seidel, R. (1983). On the shape of a set of points in the plane. *IEEE Transactions on Information Theory*, *29*(4), 551–559. https://doi.org/10.1109/tit.1983.1056714

Eder, M., Raith, S., Jalali, J., Volf, A., Settles, M., Machens, H.-G., & Kovacs, L. (2014). Comparison of different material models to simulate 3-d breast deformations using finite element analysis. *Annals of Biomedical Engineering*, *42*(4), 843–857. https://doi.org/10.1007/s10439-013-0962-8

Gall, J., Rosenhahn, B., & Seidel, H. P. (2008). Drift-free tracking of rigid and articulated objects. *2008 IEEE Conference on Computer Vision and Pattern Recognition*. https://doi.org/10.1109/cvpr.2008.4587558

Gao, F., & Han, L. (2010). Implementing the nelder-mead simplex algorithm with adaptive parameters. *Computational Optimization and Applications*, *51*(1), 259–277. https://doi.org/10.1007/s10589-010-9329-3

Garland, M., & Heckbert, P. S. (1997). Surface simplification using quadric error metrics. *Proceedings of the 24th annual conference on Computer graphics and interactive techniques - SIGGRAPH '97*. https://doi.org/10.1145/258734.258849

Gefen, A., & Dilmoney, B. (2007). Mechanics of the normal woman's breast. *Technology and Health Care*, *15*(4), 259–271. https://doi.org/10.3233/thc-2007-15404

Golyanik, V., Taetz, B., Reis, G., & Stricker, D. (2016). Extended coherent point drift algorithm with correspondence priors and optimal subsampling. *2016 IEEE Winter Conference on Applications of*

Computer Vision (WACV). https://doi.org/10.1109/wacv.2016.7477719

Greenbaum, A., Heslop, T., Morris, J., & Dunn, K. (2003). An investigation of the suitability of bra fit in women referred for reduction mammaplasty. *British Journal of Plastic Surgery*, *56*(3), 230–236. https://doi.org/10.1016/s0007-1226(03)00122-x

Haake, S., & Scurr, J. (2010). A dynamic model of the breast during exercise. *Sports Engineering*, *12*(4), 189–197. https://doi.org/10.1007/s12283-010-0046-z

Haake, S., & Scurr, J. (2011). A method to estimate strain in the breast during exercise. *Sports Engineering*, *14*(1), 49–56. https://doi.org/10.1007/s12283-011-0071-6

Han, L., Hipwell, J. H., Tanner, C., Taylor, Z., Mertzanidou, T., Cardoso, J., Ourselin, S., & Hawkes, D. J. (2011). Development of patient-specific biomechanical models for predicting large breast deformation. *Physics in Medicine and Biology*, *57*(2), 455–472. https://doi.org/10.1088/0031-9155/57/2/455

Han, L., Noble, J., & Burcher, M. (2003). A novel ultrasound indentation system for measuring biomechanical properties of in vivo soft tissue. *Ultrasound in Medicine & Biology*, *29*(6), 813–823. https://doi.org/10.1016/s0301-5629(02)00776-7

Harris, C. R., Millman, K. J., van der Walt, S. J., Gommers, R., Virtanen, P., Cournapeau, D., Wieser, E., Taylor, J., Berg, S., Smith, N. J., Kern, R., Picus, M., Hoyer, S., van Kerkwijk, M. H., Brett, M., Haldane, A., del Río, J. F., Wiebe, M., Peterson, P., ... Oliphant, T. E. (2020). Array programming with NumPy. *Nature*, *585*(7825), 357–362. https://doi.org/10.1038/s41586-020-2649-2

He, Y., Ma, L., Jiang, Z., Tang, Y., & Xing, G. (2021). Vi-eye: Semantic-based 3d point cloud registration for infrastructure-assisted autonomous driving. *Proceedings of the 27th Annual International Conference on Mobile Computing and Networking*. https://doi.org/10.1145/3447993.3483276

Hipwell, J. H., Vavourakis, V., Han, L., Mertzanidou, T., Eiben, B., & Hawkes, D. J. (2016). A review of biomechanically informed breast image registration. *Physics in Medicine and Biology*, *61*(2), R1–R31. https://doi.org/10.1088/0031-9155/61/2/r1

Hirose, O. (2021). A bayesian formulation of coherent point drift. *IEEE Transactions on Pattern Analysis and Machine Intelligence*, *43*(7), 2269–2286. https://doi.org/10.1109/tpami.2020.2971687

Huang, X., Mei, G., Zhang, J., & Abbas, R. (2021). A comprehensive survey on point cloud registration. *ArXiv*. https://doi.org/10.48550/arXiv.2103.02690

ISO 8559-1:2017. (2017). *Size designation of clothes - part 1: Anthropometric definitions for body measurement* (Standard). International Organization for Standardization. Geneva, CH.

Kalra, A., & Lowe, A. (2016). An overview of factors affecting the skins youngs modulus. *Journal of Aging Science*, *4*(2), 1000156–1000160. https://doi.org/10.4172/2329-8847.1000156

Kazhdan, M., Bolitho, M., & Hoppe, H. (2006). Poisson surface reconstruction. *Proceedings of the fourth Eurographics symposium on Geometry processing*, *7*. https://doi.org/10.2312/SGP/SGP06/061-070

Kenta-Tanaka. (2019). *Probreg* (Version 0.1.6). https://probreg.readthedocs.io/en/latest/

Khaniki, H. B., Ghayesh, M. H., Chin, R., & Amabili, M. (2023). Hyperelastic structures: A review on the mechanics and biomechanics. *International Journal of Non-Linear Mechanics*, *148*, 104275. https://doi.org/10.1016/j.ijnonlinmec.2022.104275

Khoshelham, K. (2016). Closed-form solutions for estimating a rigid motion from plane correspondences extracted from point clouds. *ISPRS Journal of Photogrammetry and Remote Sensing*, *114*, 78–91. https://doi.org/10.1016/j.isprsjprs.2016.01.010

Kim, S., & Kang, T. (2003). Garment pattern generation from body scan data. *Computer-Aided Design*, *35*(7), 611–618. https://doi.org/10.1016/s0010-4485(02)00081-7

Kleiner, B., Munkelt, C., Thorhallsson, T., Notni, G., Kühmstedt, P., & Schneider, U. (2014). Handheld 3-d scanning with automatic multi-view registration based on visual-inertial navigation. *International Journal of Optomechatronics*, *8*(4), 313–325. https://doi.org/10.1080/15599612.2014.942931

Kovnatsky, A., Bronstein, M. M., Bronstein, A. M., Glashoff, K., & Kimmel, R. (2013). Coupled quasi-harmonic bases. *Computer Graphics Forum*, *32*(2pt4), 439–448. https://doi.org/10.1111/cgf.12064

Lee, H., Hong, K., Kim, J., & Lee, S. (2001). Development of design parameters of brassiere: Part 1. three dimensional shape of the breast and under-wire of the brassiere. *Proceedings of Joint World Conference; Korea Society of Clothing and Textiles/International Textile and Apparel Association*, 90.

Lee, H. Y., Hong, K., & Kim, E. (2004). Measurement protocol of women's nude breasts using a 3d scanning technique. *Applied Ergonomics*, *35*(4), 353–359. https://doi.org/10.1016/j.apergo.2004.03.004

Lee, J., & Ashdoon, S. P. (2005). Upper body surface change analysis using 3-d body scanner. *Journal of the Korean society of clothing and textiles*, *29*(12), 1595–1607.

Logan, D. (2012). *A first course in the finite element method*. Cengage Learning.

Martínez-Martínez, F., Rupérez-Moreno, M., Martínez-Sober, M., Solves-Llorens, J., Lorente, D., Serrano-López, A., Martínez-Sanchis, S., Monserrat, C., & Martín-Guerrero, J. (2017). A finite element-based machine learning approach for modeling the mechanical behavior of the breast tissues under compression in real-time. *Computers in Biology and Medicine*, *90*, 116–124. https://doi.org/10.1016/j.compbiomed.2017.09.019

Mason, B. R., Page, K. A., & Fallon, K. (1999). An analysis of movement and discomfort of the female breast during exercise and the effects of breast support in three cases. *Journal of Science and Medicine in Sport*, *2*(2), 134–144. https://doi.org/10.1016/s1440-2440(99)80193-5

McGhee, D. E., & Steele, J. R. (2010). Optimising breast support in female patients through correct bra fit. a cross-sectional study. *Journal of Science and Medicine in Sport*, *13*(6), 568–572. https://doi.org/10.1016/j.jsams.2010.03.003

McGhee, D. E., & Steele, J. R. (2020). Breast biomechanics: what do we really know? *Physiology*, *35*(2), 144–156. https://doi.org/10.1152/physiol.00024.2019

McGhee, D. E., Steele, J. R., Zealey, W. J., & Takacs, G. J. (2013). Bra–breast forces generated in women with large breasts while standing and during treadmill running: Implications for sports bra design. *Applied Ergonomics*, *44*(1), 112–118. https://doi.org/10.1016/j.apergo.2012.05.006

Myronenko, A., & Song, X. B. (2010). Non-rigid point set registration: Coherent point drift. *IEEE Transactions on Pattern Analysis and Machine Intelligence*, *32*(12), 2262–2275. https://doi.org/10.1109/tpami.2010.46

Myronenko, A., Song, X. B., & Carreira-Perpiñán, M. (2006). Non-rigid point set registration: Coherent point drift. In B. Schölkopf, J. Platt, & T. Hoffman (Eds.), *Advances in neural information processing systems*. MIT Press. https://proceedings.neurips.cc/paper/2006/file/3b2d8f129ae2f408f2153cd9ce663043-Paper.pdf

Nasir, S. H., Troynikov, O., & Watson, C. (2015). Skin deformation behavior during hand movements and their impact on functional sports glove design. *Procedia Engineering*, *112*, 92–97. https://doi.org/10.1016/j.proeng.2015.07.181

Novak, B., Možina, J., & Jezeršek, M. (2014). 3d laser measurements of bare and shod feet during walking. *Gait & Posture*, *40*(1), 87–93. https://doi.org/10.1016/j.gaitpost.2014.02.015

Page, K. A., & Steele, J. (1999). Breast motion and sports brassiere design. *Sports Medicine*, *27*(4), 205–211. https://doi.org/10.2165/00007256-199927040-00001

Park, S. Y., Baek, J., & Moon, J. (2010a). Hand-held 3d scanning based on coarse and fine registration of multiple range images. *Machine Vision and Applications*. https://doi.org/10.1007/s00138-010-0248-1

Park, S. Y., Choi, S. I., Kim, J., & Chae, J. S. (2010b). Real-time 3d registration using GPU. *Machine Vision and Applications*, *22*(5), 837–850. https://doi.org/10.1007/s00138-010-0282-z

Parker, K. J., Doyley, M. M., & Rubens, D. J. (2012). Corrigendum: Imaging the elastic properties of tissue: The 20 year perspective. *Physics in Medicine and Biology*, *57*(16), 5359–5360. https://doi.org/10.1088/0031-9155/57/16/5359

Pei, J., Griffin, L., Ashdown, S. P., & Fan, J. (2020). The detection of the upper boundary of breasts using 4d scanning technology. *International Journal of Fashion Design, Technology and Education*, *14*(1), 1–11. https://doi.org/10.1080/17543266.2020.1829097

Pei, J., Griffin, L., Ashdown, S. P., & Fan, J. (2021a). Monitoring dynamic breast measurements obtained from 4d body scanning. *International Journal of Clothing Science and Technology*, *33*(5), 740–759. https://doi.org/10.1108/ijcst-10-2020-0157

Pei, J., Griffin, L., Ashdown, S. P., Fan, J., Juhnke, B., & Curry, C. (2021b). An exploratory study of bust measurements during running using 4d scanning technology. *International Journal of Fashion Design, Technology and Education*, *14*(3), 302–313. https://doi.org/10.1080/17543266.2021.1938699

Pinto, P., Snehal, Hipwell, J., Mccormack, V., Tanner, C., Moss, S., Wilkinson, L., Khoo, L., Pagliari, C., Skippage, P., Kliger, C., Hawkes, D., & Dos Santos Silva, I. (2010). Automated registration of diagnostic to prediagnostic x-ray mammograms: Evaluation and comparison to radiologists' accuracy. *Medical Physics*, *37*(9), 4530–4539. https://doi.org/10.1118/1.3457470

Pons-Moll, G., Romero, J., Mahmood, N., & Black, M. J. (2015). Dyna: A model of dynamic human shape in motion. *ACM Transactions on Graphics*, *34*(4), 1–14. https://doi.org/10.1145/2766993

Ramalingam, S., & Taguchi, Y. (2013). A theory of minimal 3d point to 3d plane registration and its generalization. *International Journal of Computer Vision*, *102*(1-3), 73–90. https://doi.org/10.1007/s11263-012-0576-x

Ramião, N., Martins, P., Rynkevic, R., Fernandes, A., Barroso, M., & Santos, D. (2016). Biomechanical properties of breast tissue, a state-of-the-art review. *Biomechanics and Modeling in Mechanobiology*, *15*(5), 1307–1323. https://doi.org/10.1007/s10237-016-0763-8

Rasoulian, A., Rohling, R., & Abolmaesumi, P. (2012). Group-wise registration of point sets for statistical shape models. *IEEE Transactions on Medical Imaging*, *31*(11), 2025–2034. https://doi.org/10.1109/tmi.2012.2202913

Reynaldi, A., Lukas, S., & Margaretha, H. (2012). Backpropagation and levenberg-marquardt algorithm for training finite element neural network. *2012 Sixth UKSim/AMSS European Symposium on Computer Modeling and Simulation*. https://doi.org/10.1109/ems.2012.56

Risius, D., Milligan, A., Mills, C., & Scurr, J. (2015). Multiplanar breast kinematics during different exercise modalities. *European Journal of Sport Science*, *15*(2), 111–117. https://doi.org/10.1080/17461391.2014.928914

Rueckert, D., Sonoda, L., Hayes, C., Hill, D., Leach, M., & Hawkes, D. (1999). Nonrigid registration using free-form deformations: Application to breast mr images. *IEEE Transactions on Medical Imaging*, *18*(8), 712–721. https://doi.org/10.1109/42.796284

Samani, A., Bishop, J., Luginbuhl, C., & Plewes, D. (2003). Measuring the elastic modulus of ex vivo small tissue samples. *Physics in Medicine and Biology*, *48*(14), 2183–2198. https://doi.org/10.1088/0031-9155/48/14/310

Samani, A., & Plewes, D. (2004). A method to measure the hyperelastic parameters of ex vivo breast tissue samples. *Physics in Medicine and*

Biology, *49*(18), 4395–4405. https://doi.org/10.1088/0031-9155/49/18/014

Samani, A., & Plewes, D. (2007). An inverse problem solution for measuring the elastic modulus of intact ex vivo breast tissue tumours. *Physics in Medicine and Biology*, *52*(5), 1247–1260. https://doi.org/10.1088/0031-9155/52/5/003

Sarvazyan, A. P., Skovoroda, A. R., Emelianov, S. Y., Fowlkes, J. B., Pipe, J. G., Adler, R. S., Buxton, R., & Carson, P. L. (1995). *Acoustical imaging* (Vol. 21). Springer.

Scurr, J., White, J., & Hedger, W. (2009). Breast displacement in three dimensions during the walking and running gait cycles. *Journal of Applied Biomechanics*, *25*(4), 322–329. https://doi.org/10.1123/jab.25.4.322

Scurr, J., White, J., & Hedger, W. (2011). Supported and unsupported breast displacement in three dimensions across treadmill activity levels. *Journal of Sports Sciences*, *29*(1), 55–61. https://doi.org/10.1080/02640414.2010.521944

Sohn, M., & Bye, E. (2014). Exploratory study on developing a body measurement method using motion capture (B. E. 20. Sohn MH, Ed.). *Clothing and Textiles Research Journal*, *32*(3), 170–185. https://doi.org/10.1177/0887302x14526302

Song, X.-x., & Feng, X.-w. (2006). Relationship between garment pressure and human body comfortableness. *Journal of Textile Research*, *27*(3), Article 103, 103. http://www.fzxb.org.cn/EN/abstract/article_6499.shtml

Starr, C., Branson, D., Shehab, R., Farr, C., Ownbey, S., & Swinney, J. (2005). Biomechanical analysis of a prototype sports bra. *Journal of Textile and Apparel, Technology and Management*, *4*, 1–14.

Sullivan, C., & Kaszynski, A. (2019). PyVista: 3d plotting and mesh analysis through a streamlined interface for the visualization toolkit (VTK). *Journal of Open Source Software*, *4*(37), 1450. https://doi.org/10.21105/joss.01450

Sun, Y. et al. (2019a). *Finite element model for predicting the pressure comfort and shaping effect of wired bras* (Doctoral dissertation). Hong Kong Polytechnic University.

Sun, Y., Chen, L. H., Yick, K. L., Yu, W., Lau, N., & Jiao, W. Z. (2019b). Optimization method for the determination of mooney-rivlin material coefficients of the human breasts in-vivo using static and dynamic finite element models. *Journal of the Mechanical Behavior of Biomedical Materials*, *90*, 615–625. https://doi.org/10.1016/j.jmbbm.2018.11.016

Sun, Y., Yick, K. L., Cai, Y. Q., Yu, W., Chen, L. H., Lau, N., & Zhang, S. C. (2021). Finite element analysis on contact pressure and 3d breast deformation for application in women's bras. *Fibers and Polymers*, *22*(10), 2910–2921. https://doi.org/10.1007/s12221-021-0878-0

Sun, Y., Yick, K. l., Yu, W., Chen, L., Lau, N., Jiao, W. Z., & Zhang, S. C. (2019c). 3d bra and human interactive modeling using finite element method for bra design. *Comput.-Aided Des.*, *114*, 13–27. https://doi.org/10.1016/j.cad.2019.04.006

Unlu, M. Z., Krol, A., Coman, I. L., Mandel, J. A., Baum, K. G., Lee, W., Lipson, E. D., & Feiglin, D. H. (2005). Deformable model for 3d intramodal nonrigid breast image registration with fiducial skin markers. In J. M. Fitzpatrick & J. M. Reinhardt (Eds.), *SPIE proceedings*. SPIE. https://doi.org/10.1117/12.595420

Virtanen, P., Gommers, R., Oliphant, T. E., Haberland, M., Reddy, T., Cournapeau, D., Burovski, E., Peterson, P., Weckesser, W., Bright, J., van der Walt, S. J., Brett, M., Wilson, J., Millman, K. J., Mayorov, N., Nelson, A. R. J., Jones, E., Kern, R., Larson, E., ... SciPy 1.0 Contributors. (2020). SciPy 1.0: Fundamental Algorithms for Scientific Computing in Python. *Nature Methods*, *17*, 261–272. https://doi.org/10.1038/s41592-019-0686-2

Wang, R., Xu, Y., Sotelo, M. A., Ma, Y., Gyan, T. S., Li, Z., & Li, W. (2019). A robust registration method for autonomous driving pose estimation in urban dynamic environment using LiDAR. *Electronics*, *8*(1), 43. https://doi.org/10.3390/electronics8010043

White, J., Scurr, J., & Smith, N. (2009). The effect of breast support on kinetics during overground running performance. *Ergonomics*, *52*(4), 492–498. https://doi.org/10.1080/00140130802707907

Wittek, A., Grosland, N. M., Joldes, G. R., Magnotta, V., & Miller, K. (2015). From finite element meshes to clouds of points a review of methods for generation of computational biomechanics models for patient-specific applications. *Ann. Biomed. Eng.*, *44*(1), 3–15. https://doi.org/10.1007/s10439-015-1469-2

Yang, J. (2011). The thin plate spline robust point matching (TPS-RPM) algorithm: A revisit. *Pattern Recognition Letters*, *32*(7), 910–918. https://doi.org/10.1016/j.patrec.2011.01.015

Yang, X., Chen, L., Jung, K., & You, H. (2020). Potential application of temporal 3d (4d) scanning to ergonomic design: State-of-the-art and its perspectives. *Journal of the Ergonomics Society of Korea*, *39*(1), 59–71. https://doi.org/10.5143/jesk.2020.39.1.59

Ying, S., Wang, Y., Wen, Z., & Lin, Y. (2016). Nonlinear 2d shape registration via thin-plate spline and lie group representation. *Neurocomputing*, *195*, 129–136. https://doi.org/10.1016/j.neucom.2015.07.144

Yip, J. (2016). Advanced textiles for intimate apparel. *Advances in women's intimate apparel technology* (pp. 3–23). Elsevier. https://doi.org/10.1016/b978-1-78242-369-0.00001-3

Yuan, W., Eckart, B., Kim, K., Jampani, V., Fox, D., & Kautz, J. (2020). Deepgmr: Learning latent gaussian mixture models for registration. *Computer vision – eccv 2020* (pp. 733–750). Springer International Publishing. https://doi.org/10.1007/978-3-030-58558-7_43

Yuille, A., & Grzywacz, N. (1988). The motion coherence theory. *[1988 Proceedings] Second International Conference on Computer Vision*, *3*, 344–353. https://doi.org/10.1109/ccv.1988.590011

Yuille, A., & Grzywacz, N. (1989). A mathematical analysis of the motion coherence theory. *International Journal of Computer Vision*, *3*(2), 155–175. https://doi.org/10.1007/bf00126430

Yuksel, C. (2015). Sample elimination for generating poisson disk sample sets. *Computer Graphics Forum*, *34*(2), 25–32. https://doi.org/10.1111/cgf.12538

Zhang, L. Y., Liu, Q. L., Yick, K. L., Yip, J., & Ng, S. P. (2023). Analysis of diabetic foot deformation and plantar pressure distribution of women at different walking speeds. *International Journal of Environmental Research and Public Health*, *20*(4), 3688. https://doi.org/10.3390/ijerph20043688

Zhang, S. C., Yick, K. L., Yip, J., Yu, W., & Tang, K. P. M. (2021). An understanding of bra design features to improve bra fit and design for older chinese women. *Textile Research Journal*, *91*(3-4), 406–420. https://doi.org/10.1177/0040517520944253

Zhang, X., Yeung, K., & Li, Y. (2002). Numerical simulation of 3d dynamic garment pressure. *Textile Research Journal*, *72*(3), 245–252. https://doi.org/10.1177/004051750207200311

Zheng, Y., Li, Y., Yang, S., & Lu, H. (2022). Global-PBNet: A novel point cloud registration for autonomous driving. *IEEE Transactions on Intelligent Transportation Systems*, 1–8. https://doi.org/10.1109/tits.2022.3153133

Zhou, J., Yu, W., & Ng, S. P. (2011). Methods of studying breast motion in sports bras: A review. *Textile Research Journal*, *81*(12), 1234–1248. https://doi.org/10.1177/0040517511399959

Zhou, J., Yu, W., & Ng, S. P. (2012). Studies of three-dimensional trajectories of breast movement for better bra design. *Textile Research Journal*, *82*(3), 242–254. https://doi.org/10.1177/0040517511435004

Zhou, J., Yu, W., & Ng, S. P. (2013). Identifying effective design features of commercial sports bras. *Textile Research Journal*, *83*(14), 1500–1513. https://doi.org/10.1177/0040517512464289